CONVECTIVE FLOW THROUGH POLYMER ELECTROLYTE FUEL CELLS

by

Joseph P. Feser

A thesis submitted to the Faculty of the University of Delaware in partial fulfillment of the requirements for the degree of Master of Science in Mechanical Engineering

Summer 2005

CONVECTIVE FLOW THROUGH POLYMER ELECTROLYTE FUEL CELLS

by

Joseph P. Feser

Approved: _____
Ajay K. Prasad, Ph.D.
Professor in charge of thesis on behalf of the Advisory Committee

Approved: _____
Thomas S. Buchanan, Ph.D.
Chair of the Department of Mechanical Engineering

Approved: _____
Eric W. Kaler, Ph.D.
Dean of the College of Engineering

Approved: _____
Conrado M. Gempesaw II, Ph.D.
Vice Provost for Academic and International Programs

ACKNOWLEDGEMENTS

Thank you to W.L. Gore and Associates for research funding. Specifically, I would like to thank Will Johnson, Uwe Buecher, and Wen Liu for our many thought provoking conversations and their continued encouragement. The U.S. Department of Energy also deserves recognition for funding parts of this research.

Thanks to everyone in the experimental fluids groups, but especially to Mike Manlove for helping out with the permeability experiments, Dusan Spernjak for helping to create our home-built high-magnification lens, Tom Shipman for helping to manage our lasers, and Sudhaker Chhabra for writing our PIV interrogation source code and a nice user interface.

Thank you to my advisors, Dr. Prasad and Dr. Advani, for giving me the guidance needed to reach our objectives while allowing me the freedom to experiment with new objectives entirely. I imagine it takes a little faith and a lot of patience to be my advisor, so thanks for having both. I am truly proud to be your advisee.

Most of all I owe a debt of gratitude to my fiancé. Allie, thank you for putting up with my obsession-compulsion to derive equations on every spare piece of paper in the house. Despite all this, you're willing to spend the rest of our lives together.

TABLE OF CONTENTS

LIST OF FIGURES

LIST OF TABLES

ABSTRACT

Hydrogen powered PEM fuel cells have three primary loss mechanisms: activation overpotential, ohmic overpotential, and the mass-transport limited overpotential. It is suggested that convection in the form of channel bypass can be used to increase reactant concentrations in the catalyst layer which will improve reaction kinetics. Further, if convection can be made the dominant mechanism for gas transport, the diffusion-limited mass-transport overpotential can be reduced or removed. In order to determine under what conditions this can take place, an analytic model was developed for convective flow within a single serpentine channel configuration. The model shows that the channel length and in-plane permeability of the gas diffusion layers are most important factors.

Particle Image Velocimetry was used to observe the velocity fields in representative test sections of an interdigitated and a serpentine fuel cell. Using ex-situ methods, it was shown that it is possible observe secondary flows with primary-to-secondary velocity ratios approaching 100-to-1. Channel bypass was observed in both configurations. Local variation in permeability appears to cause local variation in velocity fields in the channel.

A radial permeability experiment designed and fabricated to characterize and differentiate in-plane permeability of three gas diffusion layers manufactured by different techniques. It was shown that experiments can use either a wetting liquid or a gas of known viscosity as the host fluid and reach identical conclusions. However, flowrates' dependence on pressure is different for gases and liquids and must be recognized when large pressure differentials are present.

Chapter 1

POLYMER ELECTROLYTE MEMBRANE FUEL CELLS AND THE GAS DIFFUSION LAYER

1.1 Overview

The goal of this work is to investigate convective flow in polymer electrolyte fuel cells. To begin, the fundamental concepts needed to understand the inner-workings of a fuel cell will be presented, followed by a more detailed description of how the gas diffusion layers and the channels in a bipolar plate are related to convection. Chapter 2 will explain in detail why convection is important and then develop a simple model which predicts the conditions under which convection will be important to fuel cell operation in single serpentine flow fields as well as the effect of various geometric and material parameters. A central theme is the role of gas diffusion layer in-plane permeability on convection. In Chapter 3, particle image velocimetry is used to observe flow in the channels of the bipolar plate. Chapter 2 and 3 establish the importance of in-plane permeability; in chapter 4, an improved technique is developed to measure it. The technique is validated and subsequently, the in-plane permeability of gas diffusion layers representing the three major manufacturing techniques are measured. Chapter 5 is a brief summary of research findings and a proposal for future efforts.

1.2 PEM Fuel Cells

Fuel cells are devices that convert chemical energy from an oxidation reaction directly to electrical energy. Under practical conditions, it is possible to achieve very

high efficiencies compared to other power generating devices. Many types of fuel cells exist, each with their own advantages and disadvantages; the following work will be directed toward the class of fuel cells known as polymer electrolyte membrane fuel cells, also known as proton exchange membrane fuel cells or PEMFC's.

In hydrogen fueled PEMFC's, hydrogen is passed through channels in a bipolar plate. Hydrogen penetrates the gas diffusion layer after which it reaches the anode catalyst layer. Once there, the platinum catalyst facilitates the dissociation of hydrogen into protons and electrons. The key feature of a PEMFC is that the membrane is able to freely conduct protons while it remains relatively impermeable to electrons. Thus, protons migrate across the membrane while electrons must be conducted through an external circuit; since this process takes place under voltage, useful electrical power is generated along the way. Once the protons and electrons reach the cathode, they combine with oxygen in the presence of a platinum catalyst to form water and heat. The water and heat must then be removed through the cathode gas diffusion layer and the channels in the bipolar plate. Figure 1.1 shows the schematic of this process.

There are three major sources of inefficiency in a PEMFC: the activation overpotential, the ohmic overpotential, and the mass transport losses. Over the majority of a polarization curve, the most severe loss comes from the activation overpotential which is caused by poor reaction kinetics. It has been shown that in hydrogen PEMFCs, the cathode oxygen reduction reaction (ORR) is primarily responsible for this loss; in direct methanol PEMs the kinetics are slow on both the anode and cathode leading to the so-called double potential. The cathode electrokinetics is usually modeled by the Tafel equation which gives a relationship between the current density, the surface overpotential, and the reactant concentration under the assumption of large surface overpotential.

$$i = -i_{o,c}^{\text{ref}} \left(\frac{C_{O_2}}{C_{O_{2,ref}}} \right) \exp\left(-\frac{\alpha_c}{RT} F\eta \right) \tag{1.1}$$

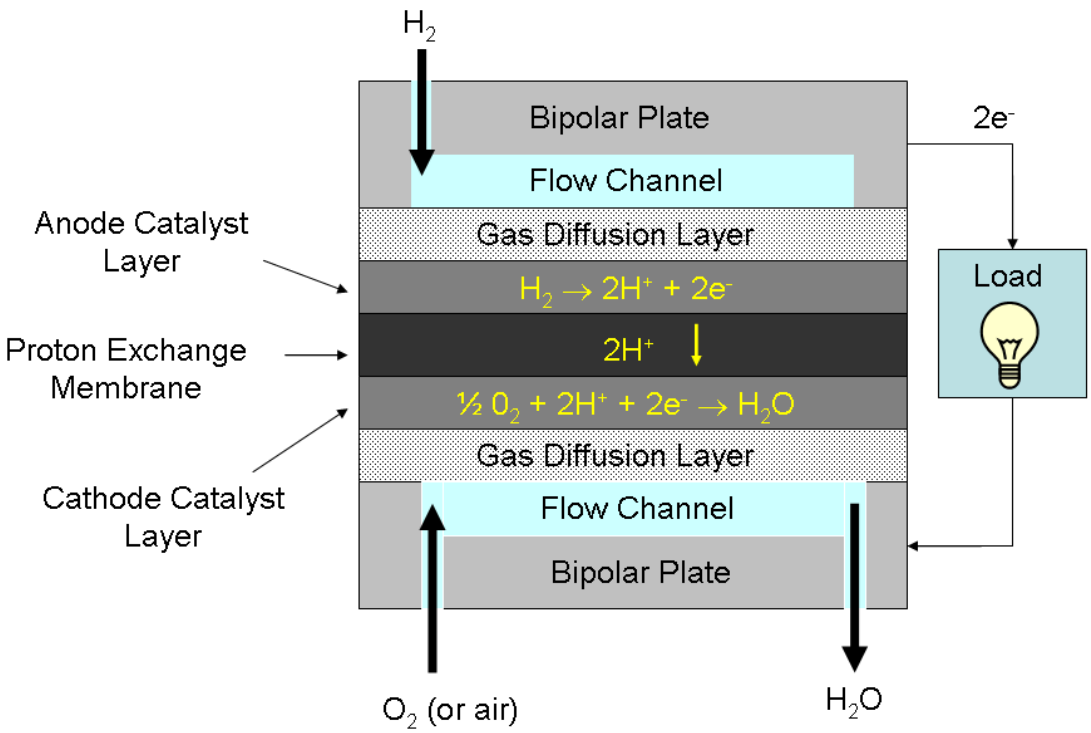

Figure 1.1: Schematic of hydrogen PEM fuel cell

where $i_{o,c}^{\text{ref}}$ is the reference exchange current density, α_c is the cathodic transfer coefficient, F is the Faraday constant, and C_{O_2} is the concentration of oxygen in the catalyst layer. The driving force of the reaction comes from the surface overpotential, η. It is a measure of how close the applied voltage is to the equilibrium potential. The further away from equilibrium, the more readily the reaction occurs. The surface overpotential can be written as

$$\eta = \Phi_{\text{electronic}} - \Phi_{\text{electrolyte}} - U_0 \tag{1.2}$$

where $\Phi_{\text{electrolyte}}$ and $\Phi_{\text{electronic}}$ are the electric potentials of the electrolyte and electronic phase respectively. U_0 is the equilibrium potential of the reaction. It is a function of the reactant concentration, according to the Nernst equation. Thus, by increasing the reactant concentration in the catalyst layer, the reaction can be driven faster for a fixed cell voltage.

The Tafel equation explains the shape of a polarization curve for a fuel cell. Region (a) in figure 1.2 shows the kinetic regime. At higher current densities, performance is further reduced by ohmic losses in the electrolyte and, to a lesser extent, in the gas diffusion layer and bipolar plate; this is shown as region (b) of figure 1.2. Mass transport losses are an effect of low concentration in the catalyst layer; this can be caused by diffusion rate limitations, by liquid water blockages, or by temporary reactant overuse during periods of rapid transients (region (c)). The current research aims to use convection as a means to raise the surface overpotential and as well reduce mass transport limitations. Since the two components that are concerned most directly with convection are the gas diffusion layers and the bipolar plates, it is relevant to describe them in more detail.

1.3 Introduction to the Gas Diffusion Layer and Bipolar Plates

The gas diffusion layer serves five key purposes: mechanical support, electronic conductivity, heat removal, reactant access to the catalyst layers, and product

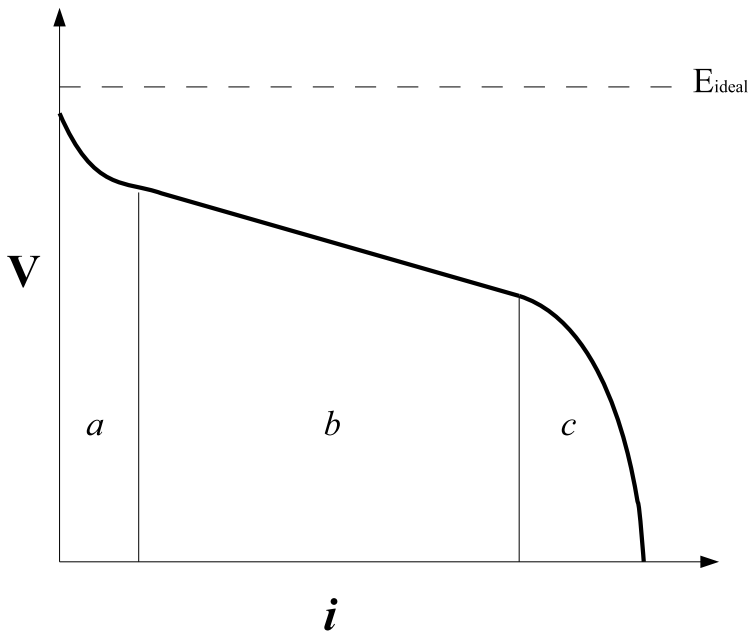

Figure 1.2: In a typical fuel cell polarization curve, the three major sources of voltage losses are a) activation overpotential caused by slow reaction kinetics b) Ohmic overpotential caused by conductive losses proportional to the current density c) Losses caused by insufficient mass transport to the catalyst layer

removal from it. It must accomplish all five of these tasks while in the corrosive environment of the fuel cell. Currently, all gas diffusion layers consist of graphitized carbon fiber which are connected according to three major classes of manufacturing techniques: woven carbon cloth, carbon fiber paper, and non-woven carbon fiber webs. A detailed review on the characterization of gas diffusion media and their manufacturing techniques was recently provided by Mathias [14]. It is generally agreed that the GDL plays only a small role in the ohmic losses of a PEM fuel cell [14]. Thus, most of the recent focus on GDL has been in the field of two phase flow which is applicable to the mass-transporting limiting regime. In order to improve their ability to control liquid water transport, many current gas diffusion media are supplemented with a highly hydrophobic microporous layer which is adjacent to the catalyst; explanations for why (or whether) the microporous layer enhances fuel cell performance continue to be debated in the literature ([28],[18],[22]).

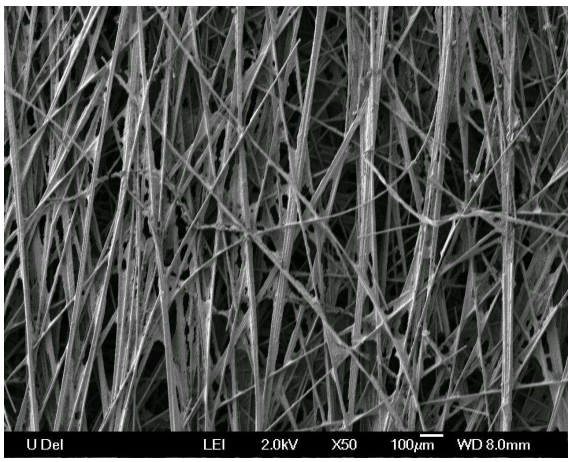

Figure 1.3: Top-view SEM Photograph of SGL31BA, a non-woven carbon fiber gas diffusion layer.

A topic which is discussed less in the literature, but may be equally important is the role of convection in the gas diffusion layer. For reasons to be discussed in the next chapter, convective flow of reactants may reduce the activation overpotential

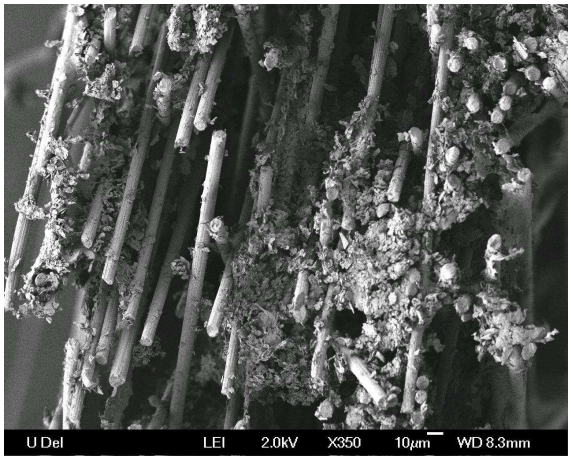

Figure 1.4: Through-Thickness SEM Photograph of SGL31BA

as well as any mass transport limited phenomenon. The material property which characterizes the ability of gas to convect in a porous medium is its permeability. This is is usually expressed through Darcy's law

$$u_i = \frac{K_{i,j}}{\mu} \frac{\partial p}{\partial x_j} \tag{1.3}$$

In general, anisotropic materials can have up to three distinctly different principal Darcy permeabilities which can vary spatially. However, in the special cases of symmetrically woven fabrics such as carbon fiber cloth and randomly oriented fiber papers it is often assumed that the material is homogenous and transversely isotropic which reduces the number of distinct permeabilities to two (the so-called through-plane and in-plane permeabilities). It is hypothesized that the in-plane and/or through-plane permeability are related to the convection into the GDL in a fuel cell; it is one of the primary objectives of this work to determine what relationship exists between permeability and convection in the GDL.

The bipolar plate serves many of the same functions as the gas diffusion layers. Its primary roles are to: 1) conduct electrons efficiently from the anode GDL to the cathode GDL 2) remove excess heat from the cell 3) distribute reactant gases

4) remove reaction products from the cell. The merits of a particular bipolar plate design are judged by its ability to perform these four tasks as well as its abilities to withstand chemical degradation, operate with few pumping requirements, and be manufactured inexpensively. Many flow channel designs have been investigated. However, there are four basic categories of channels designs that are currently popular.

The most basic design is known as the parallel configuration (see figure 1.5). In the design, inlet reactants branch into a parallel network of channels which recombine at the outlet. The primary advantage of this setup is the low pressure drop required to pump the reactant gases. However, it has the disadvantage that any flow blockage caused by product liquid water (in the case of hydrogen fuel cells) or carbon dioxide bubbles (in the case of direct methanol fuel cells) is difficult to remove because the flow will preferentially attempt to travel through the unobstructed parallel channels instead of forcing the removal of the blockage.

A design which removes blockages more readily is the single serpentine. By sending all of the reactant through a single, winding channel, any blockage will force a large pressure differential to be generated which will help to remove the blockage. However, because all of the reactant travels through a single channel, large pressures are required to achieve suitable flowrates. A modern approach which balances the need for reduced parasitic losses from pumps and increased ability for blockage removal is the emerging class of multi-serpentine networks which combine the blockage removal characteristics of single-serpentine with the low pumping requirements of the parallel system.

The fourth major bipolar plate design is the interdigitated design. By using a series of dead-ended 'fingers,' reactant is forced to convect into the GDL before reemerging into adjacent 'fingers' which lead to the outlet. The convection forced by the interdigitated design is thought to have several benefits (these will be discussed

later). Although the interdigitated design requires more pumping power than the parallel design in order to force reactant into the GDL, the extra pumping power is not as significant as that required for the serpentine configuration because the area for convective distribution is very large.

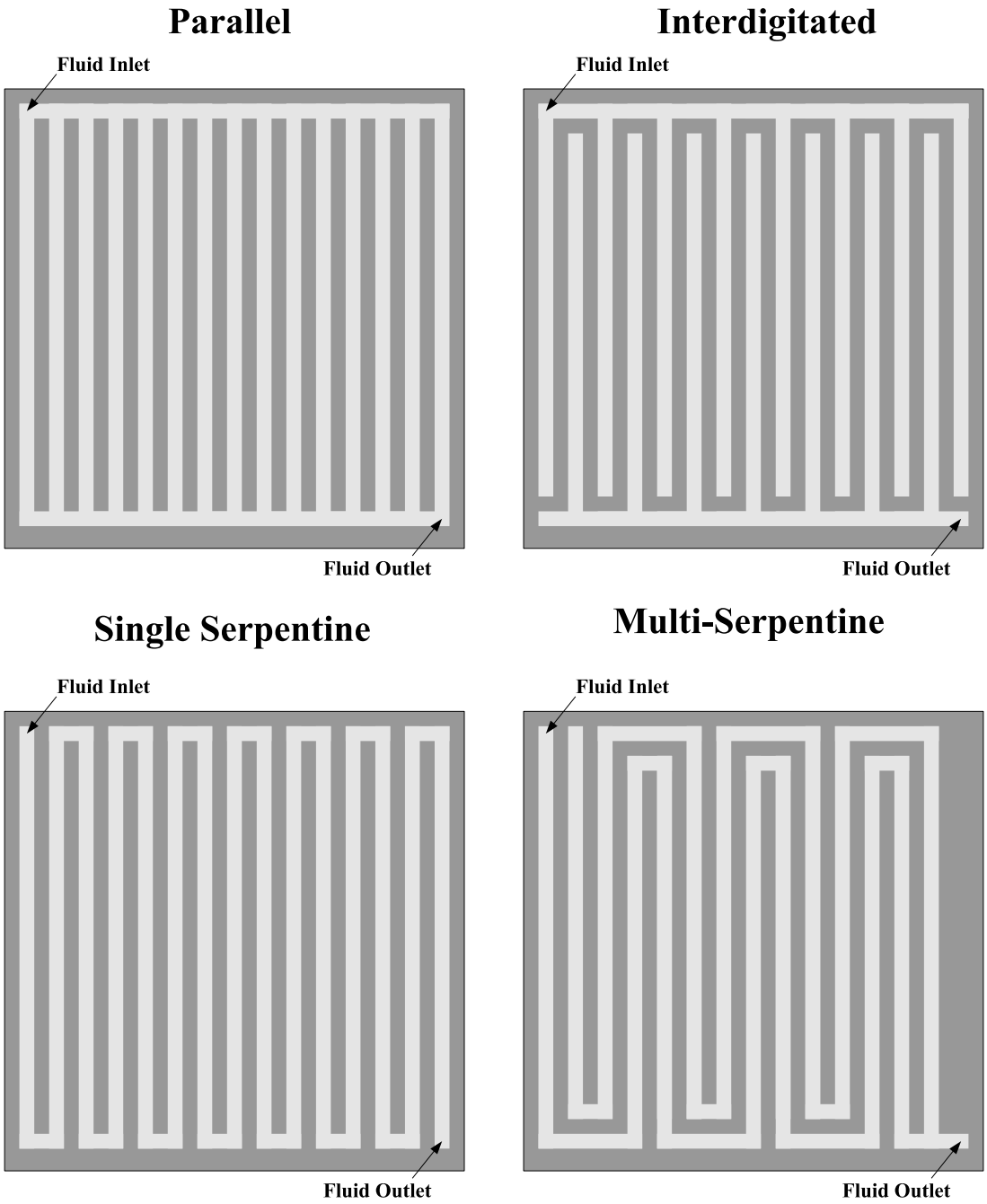

Figure 1.5: Four basic categories of channel designs for bipolar plates

Chapter 2

THE ROLE OF CONVECTION IN SINGLE SERPENTINE FLOW FIELDS

2.1 Channel-Bypass as a Mechanism for Improved Performance

One of the most widely used flow channel configurations for modern fuel cells is the single serpentine. Shown in fig. 2.1, the single serpentine consists of one continuous channel that sweeps back and forth. The single serpentine configuration forces nearly all of the reactants through a single, long channel. This is in contrast to flow channel configurations such as parallel, interdigitated, and parallel-serpentine hybrids which allow flow to be distributed over many channels whose individual lengths are much shorter. Thus a large pressure drop is necessary to generate enough flow to satisfy the stoichiometric requirements of single serpentine fuel cell.

The larger pressure drop across the single serpentine configuration presents both challenges and opportunities for cell designers. An obvious shortcoming of such a configuration is that it will require larger pumps which, before considering any increases in fuel cell performance, adversely affects both system cost and volume. However, the larger pressure drop may contribute to cell performance in several ways. First, it can enhance the ability of the cell to remove blockages such as those created by liquid water produced on the cathode side of a hydrogen fuel cell or by carbon dioxide bubbles produced on the anode side of a direct methanol fuel cell. This improves the ability of the fuel cell to operate at high current densities.

The combination of large pressure drops and channel configuration can lead to second mechanism for increased performance; that mechanism is channel bypass. Figure 2.4 contains a schematic of how the mechanism works. Any pressure difference between adjacent channels can cause a velocity field from one channel to the other through the GDL. In a single serpentine flow field, this pressure differential can be generated by viscous losses associated with high velocity fluid travelling through the channel.

In order to understand why channel bypass might be advantageous to fuel cell performance consider the two primary mechanisms for mass transport in fuel cells, binary diffusion and convection. In diffusion, "Brownian" motion causes molecules to randomly distribute; the concentration flux due to diffusion j_{diff} is usually described as being driven by a concentration gradient. Then according to Fick's law,

$$j_{\text{diff}} = -D\nabla c \tag{2.1}$$

where D is the binary diffusion coefficient and c is the species concentration. What is important to notice is that a loss in concentration is necessary to drive mass transport by diffusion.

In convection, molecules are physically carried at the local velocity, $\tilde{u}$; thus net flux of molecules of a particular species due to convection is given by

$$j_{conv} = c\tilde{u} \tag{2.2}$$

In contrast to diffusion, convection does not necessarily require a loss in concentration. This is the key reason why convection is desirable over diffusion. The net flux of molecules due to the combination of convection and diffusion is merely the sum of the two fluxes.

$$j_{net} = c\tilde{u} - D\nabla c \tag{2.3}$$

In the absence of a velocity field (no convection), a definite limiting mass flux (and thus limiting current) exists, because the largest concentration gradient that can

possibly exist for a given channel concentration, c_{chan}, occurs when the catalyst layer has $c = 0$, so that $j_{\text{diff,max}} = -Dc_{\text{chan}}/t$, where t is the thickness of the gas diffusion layer. In reality, even this limiting flux is not reached in a fuel cell because at low concentrations of react the cell will perform so poorly that the point of maximum power density would be crossed. Any current density (mass flux) beyond that point is useless because the same power density could be achieved with less mass transport. By contrast, since convection does not require large concentration losses, higher reactant concentrations can be achieved in the catalyst layer when this is the dominant mechanism. Channel bypass is postulated to be a means by which to enhance cell performance by changing the dominant mode of mass transport from diffusion to convection. This has long been known of interdigitated flow fields ([27],[17],[6],[7],[25]), but has yet to be proven conclusively for single serpentine flow fields.

2.2 Formulation

In order to show the significance of convection in single serpentine flow fields, we developed a simple model which can predict the velocity profile. To start, consider the design of a typical single serpentine flow field. Many current serpentine designs employ channels that are approximately 1mm wide with land regions that are also about 1mm wide. Thus even for a small cell area of the order of 10 cm^2, the serpentine makes about 16 180° turns. One expects, given the repetitive nature of the serpentine geometry, that after a period of development, the flow will settle to a spatially periodic velocity field. Then, the analysis can be restricted to a unit cell within the fully developed region. Figure 2.1 shows a representative section of the channel.

The velocity in the channel is three dimensional; in the most general formulation it is possible to search for the velocity in the primary flow direction, $u(x, y, z)$, as well as the secondary flows, $v(x, y, z)$ and $w(x, y, z)$, which must be present in

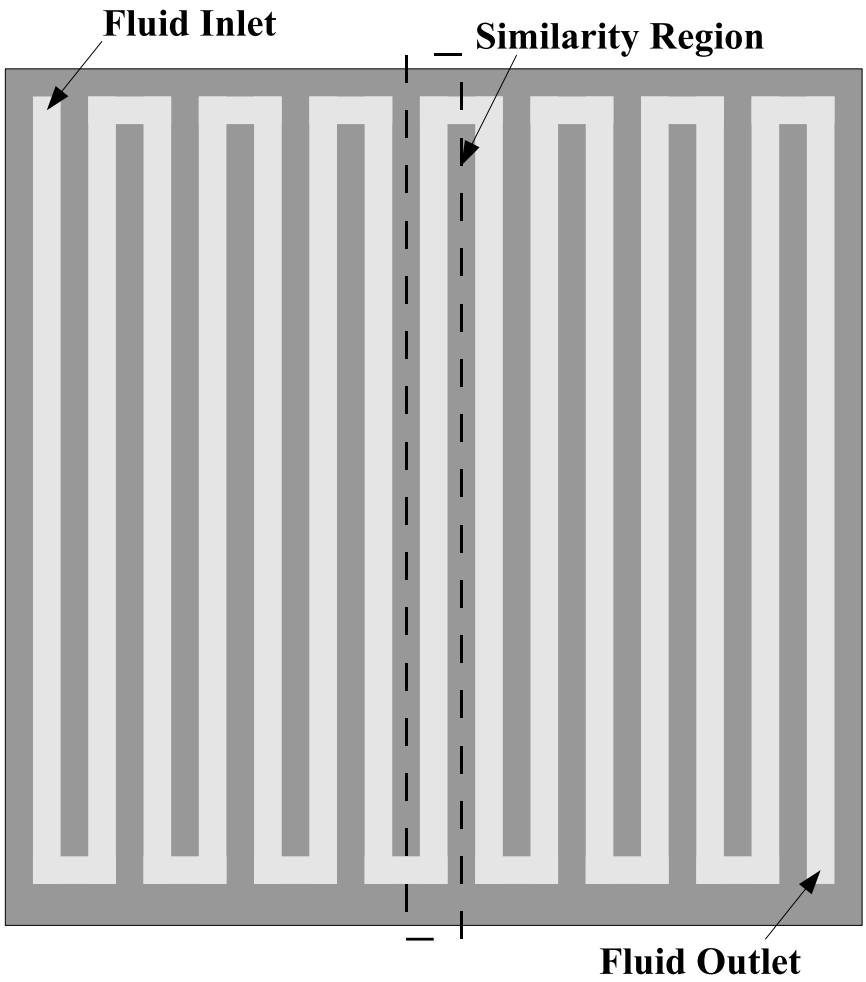

Figure 2.1: A few channels after the inlet, it is anticipated that the flow reaches a periodically defined field. A region of similarity is shown in the dashed box. Equations 2.8-2.10 can be used to relate the velocity in adjacent similarity regions.

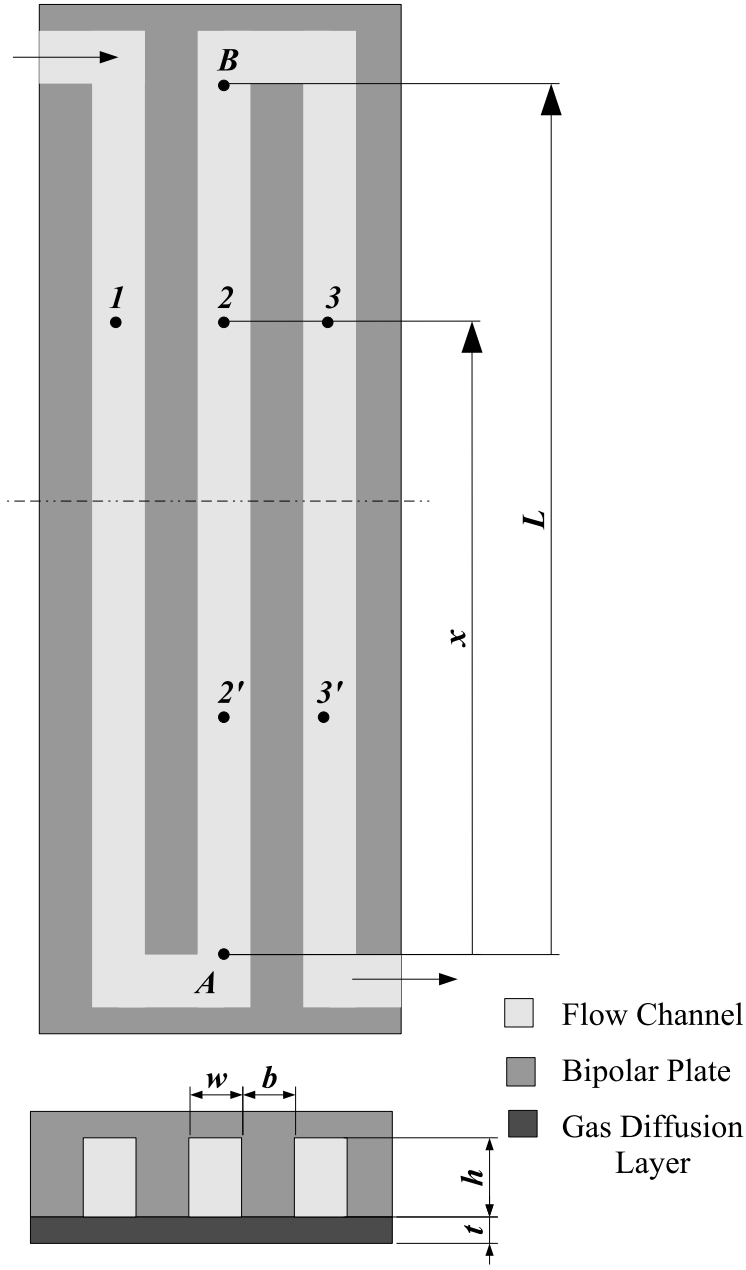

Figure 2.2: Unit cell of an infinitely extended serpentine. The analytic formulation attempts to solve for pressure and velocity field of the central channel. The points shown (1-3,2'-3') are used to develop symmetry conditions.

order for channel bypass to occur. Computer software has been used to solve the full set of Navier-Stokes equations in the flow channels with Darcy's Law applied in the porous media by use of a source term which is only non-zero in the GDL. While computer solutions have the advantage of being able to simulate the full three dimensional flow at high Reynolds number, they are limited in that they are time consuming and can only be performed for a finite number of parameter values. An analytic solution for the full three dimensional flow at high Reynolds number would be difficult if not impossible, but under some simplifications, an analytic solution is possible that contains most of the useful information from the computational solution.

The most important simplification is that gas in the flow channels and GDL remains at constant density and viscosity. In a fuel cell, this is never truly the case because some portion of the gas will always be consumed by the chemical reaction. However, if the model is restricted to represent the cathode of an air-breathing fuel cell, the simplification becomes more realistic. Air is composed of 78% Nitrogen and only 20% Oxygen. Thus, even if the chemical reaction completely consumes a fuel cell's oxygen, the vast majority of the inlet gas remains. However,for practical fuel cell applications oxygen is never allowed to deplete entirely as it would severely hinder cell efficiency. Viscosity is strongly dependent on temperature; however, computer modeling work indicates that the fluctuations in temperature are small enough to neglect local changes in viscosity [24]. The assumption of constant density and viscosity may also be applicable on the anode of a direct methanol fuel cell for analogous reasons.

In order to further simplify the analysis, assume that the magnitude of secondary velocities, v and w, are much smaller than the velocity along the direction of the channel, u. Also assume that u varies slowly with x and that the pressure p varies slowly with y and z so that the first of the Navier-Stokes equations reduces

to the unidirectional form

$$\frac{\partial^2 u}{\partial y^2} + \frac{\partial^2 u}{\partial z^2} = \frac{1}{\mu}\frac{dP}{dx} \tag{2.4}$$

The no-slip condition can then be applied to u at the boundaries of the channel cross section. Equation 2.4 is of Poisson form and solutions are available for most geometries of importance. Regardless of the specific geometry of the flow channel, the average velocity in the channel can always be expressed in the form

$$u_{mean} = -f\frac{A_c}{\mu}\frac{dP}{dx} \tag{2.5}$$

where A_c is the cross sectional area of the channel and f is a non-dimensional function of non-dimensional groups which defines the geometry of the channel, but may also include provisions for a portion of the GDL which protrudes into the channel. The term fA_c can be viewed as the 'permeability' of the channel, hereon denoted as k_c. The flow channel geometry most often employed is rectangular. In this case, $A_c = wh$, where w is the width of the channel and h is the height; the function $f = f(h/w)$ can be tabulated numerically and is shown in fig. 2.3 (solved in-house by an implicit finite difference scheme).

An expression similar to eq. 2.5 can be obtained to relate the channel by-pass to the pressure drop between adjacent channels can be established from first principles. Figure 2.4 shows a characteristic cross-section of a fuel cell. It can be shown that the total flowrate travelling under the land is always linearly related to pressure drop between the two channels. Then the average artificial velocity, v_{gdl}, under a land of width b can be expressed as

$$v_{gdl} = \frac{k_{\text{eff}}}{\mu}\frac{P_{high} - P_{low}}{b} \tag{2.6}$$

where the subscript on the permeability takes into account the geometric layout of

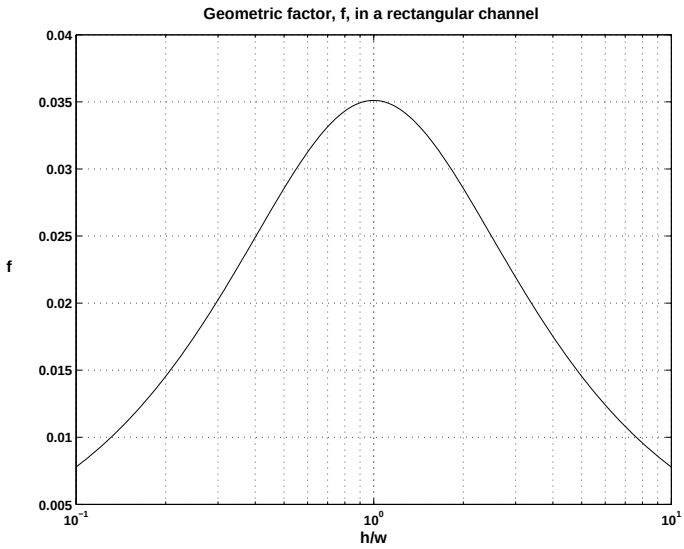

Figure 2.3: Non-dimension function, $f\left(\frac{h}{w}\right)$, which describes the permeability of a rectangular channel (see equation 2.5). Values determined from numerical solution of equation 2.4.

the problem as well as any difference in the in-plane permeability, k_i, and through-plane permeability, k_t, of the GDL. However, the effective permeability, k_{eff} approaches the in-plane permeability under the condition

$$\frac{k_i}{k_t}\frac{t^2}{b^2} \ll 1 \tag{2.7}$$

A typical value of the ratio $\frac{t}{b}$ is 0.2-0.4. Based on reported values of through-plane permeability in the literature [14] and in-plane permeability values reported later in the current study, the ratio $\frac{k_i}{k_t} \approx 1$ for at least two commonly used GDL materials (TGP-060-H paper and Avcarb 1071-HCB cloth). Thus, inequality 2.7 is satisfied for a wide range of applications.

In order to proceed further, one must consider the symmetries of the infinite serpentine. The computational solution of the complete 3D equations of motion recently presented by [20] uses a double pass of the channel as the repeating unit for symmetry; while this does give a correct solution, a smaller repeating unit of only

one pass can be used, if the periodic boundary conditions are altered slightly. To obtain the flow in the subsequent (counterflow) channel, all one needs to do is use the transformation

$$u_{adj}(x) = -u(L-x) \tag{2.8}$$

$$v_{adj}(x) = v(L-x) \tag{2.9}$$

$$P_{adj}(x) = P(L-x) + P(L) \tag{2.10}$$

where hereon the subscripts on u and v have been dropped and are understood to represent the mean value in the channel and GDL respectively.

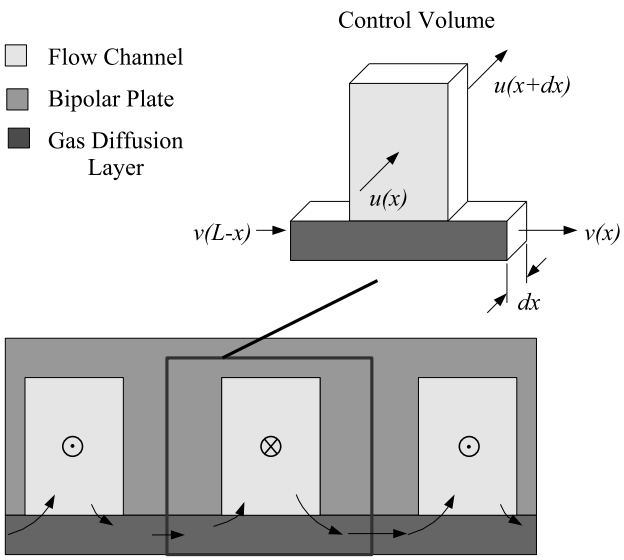

Figure 2.4: Control volume used to develop continuity equation. Velocity entering from left side of GDL is $v(L-x)$ because of the relationship in eq. 2.9.

A control volume (shown in fig. 2.4) can be defined which encompasses the flow channel and GDL over the width of one channel and has infinitesimal depth in the x direction. The only mass fluxes on the control volumes boundaries come from

the u component of velocity in the channel and the v component of velocity in the GDL. Then, for mass conservation

$$A_c \frac{du}{dx} + t\left(v(x) - v(L-x)\right) = 0 \tag{2.11}$$

The expression for $u(x)$ is given by equation 2.5. Using the simplified version of equation 2.6 in conjunction with figure 2.2, the GDL velocities can be obtained as

$$v(x) = \frac{k_i}{\mu b}(P_2 - P_3) \tag{2.12}$$

$$v(L-x) = \frac{k_i}{\mu b}(P_{2'} - P_{3'}) \tag{2.13}$$

But using equation 2.10 to relate the pressures in adjacent channels,

$$P_3 = P_{2'} + P(L) \tag{2.14}$$

$$P_{3'} = P_2 + P(L) \tag{2.15}$$

This information can be used in the continuity equation to arrive at the combined equation

$$\frac{d^2P(x)}{dx^2} + \frac{2}{A_c}\frac{t}{b}\frac{k_i}{k_c}(P(L-x) - P(x)) = 0 \tag{2.16}$$

If the total change in pressure over the entire cell is given by ΔP_{cell} and the total number of channel passes is N_c, then the boundary conditions on equation 2.16 are given by

$$P(0) = 0 \tag{2.17}$$

$$P(L) = \frac{\Delta P_{cell}}{N_c} \tag{2.18}$$

2.3 Solution

Equation 2.16 is unique in that the arguments that appear in the pressure are not all the same. Equations of this type are usually encountered as initial value problems rather than boundary value problems, where the argument can be

interpreted as a 'time' delay. In the current case, the argument does not represent a delay, but rather an offset that is indicative of the symmetry. In order to obtain the solution, consider the change of variable $\bar{P}(x) = P(x) - \frac{\Delta P_{cell}}{2N_c}$ and $\bar{x} = \frac{x}{L} - \frac{1}{2}$. Then, the governing equation becomes.

$$\frac{d^2\bar{P}}{d\bar{x}^2}(L/2 + L\bar{x}) + \frac{m^2}{2}(\bar{P}(L/2 - L\bar{x}) - \bar{P}(L\bar{x} + L/2)) = 0 \tag{2.19}$$

with boundary conditions

$$\bar{P}(0) = -\frac{\Delta P_{cell}}{2N_c} \tag{2.20}$$

$$\bar{P}(L) = \frac{\Delta P_{cell}}{2N_c} \tag{2.21}$$

where

$$m^2 = 4\frac{L^2}{A_c}\frac{t}{b}\frac{k_i}{k_c} \tag{2.22}$$

In eq. 2.16-2.21 the argument is still in x. However, due to the special form of 2.16, a change of argument $\bar{P}(x) \to \bar{P}(\bar{x})$ yields the simplified form.

$$\frac{d^2\bar{P}}{d\bar{x}^2}(\bar{x}) + \frac{m^2}{2}(\bar{P}(-\bar{x}) - \bar{P}(\bar{x})) = 0 \tag{2.23}$$

with boundary conditions

$$\bar{P}(-1/2) = -\frac{\Delta P_{cell}}{2N_c} \tag{2.24}$$

$$\bar{P}(1/2) = \frac{\Delta P_{cell}}{2N_c} \tag{2.25}$$

If equation 2.23 is evaluated at an arbitrary point, $\bar{x} = \xi$, on the interval $[-1/2, 1/2]$, then

$$\frac{d^2\bar{P}}{d\bar{x}^2}(\xi) + \frac{m^2}{2}(\bar{P}(-\xi) - \bar{P}(\xi)) = 0 \tag{2.26}$$

is satisfied. Likewise, because the interval is symmetric, the equation can always be evaluated at $\bar{x} = -\xi$ to yield

$$\frac{d^2\bar{P}}{d\bar{x}^2}(-\xi) + \frac{m^2}{2}(\bar{P}(\xi) - \bar{P}(-\xi)) = 0 \tag{2.27}$$

Adding equations 2.26 and 2.27 and recognizing that since ξ was arbitrary, the resulting equation will hold for all $\bar{x}$:

$$\frac{d^2\bar{P}}{d\bar{x}^2}(\bar{x}) = -\frac{d^2\bar{P}}{d\bar{x}^2}(-\bar{x}) \tag{2.28}$$

Integrating equation 2.28

$$\frac{d\bar{P}}{d\bar{x}}(\bar{x}) = \frac{d\bar{P}}{d\bar{x}}(-\bar{x}) + C_1 \tag{2.29}$$

However, since u should have equivalent values at the two boundaries, the derivative terms in 2.30 are equal and $C_1 = 0$. Integrating 2.29

$$\bar{P}(\bar{x}) = -\bar{P}(-\bar{x}) + C_2 \tag{2.30}$$

Since $\bar{P}(\bar{x})$ is continuous on the interval $[-1/2, 1/2]$, equation 2.30 can be evaluated at $\bar{x} = 0$ to find that $C_2 = 0$. Thus, $\bar{P}(\bar{x})$ is a symmetric function. Recognizing that the solution is symmetric, equations 2.23-2.25 simplify into the more manageable form,

$$\frac{d^2\bar{P}}{d\bar{x}^2}(\bar{x}) - m^2\bar{P}(\bar{x}) = 0 \tag{2.31}$$

with boundary conditions

$$\bar{P}(0) = 0 \tag{2.32}$$

$$\bar{P}(1/2) = \frac{\Delta P_{cell}}{2N_c} \tag{2.33}$$

These have the solution

$$\bar{P}(\bar{x}) = \frac{\Delta P_{cell}}{2N_c}\frac{\sinh(m\bar{x})}{\sinh\left(\frac{m}{2}\right)} \tag{2.34}$$

Under a change of variables and argument, the solution can be written in the original coordinate system.

$$\boxed{P(x) = \frac{\Delta P_{cell}}{2N_c}\left(\frac{\sinh\left(m\left(\frac{x}{L} - \frac{1}{2}\right)\right)}{\sinh\left(\frac{m}{2}\right)} + 1\right)} \tag{2.35}$$

Then, the mean velocity in the channel is obtained using equation 2.5.

$$\boxed{u(x) = -\frac{k_c}{2\mu L}\frac{\Delta P_{cell}}{N_c}\frac{m\cosh\left(m\left(\frac{x}{L}-\frac{1}{2}\right)\right)}{\sinh\left(\frac{m}{2}\right)}} \tag{2.36}$$

The mean artificial velocity in the GDL is given by equation 2.6.

$$v(x) = \frac{k_{\text{eff}}}{\mu b}(P(x) - P(L-x) - P(L)) \tag{2.37}$$

After some manipulation, the artificial velocity can be found to be

$$\boxed{v(x) = \frac{k_{\text{eff}}}{\mu b}\frac{\Delta P_{cell}}{N_c}\left(\frac{\sinh\left(m\left(\frac{x}{L}-\frac{1}{2}\right)\right)}{\sinh\left(\frac{m}{2}\right)} - 1\right)} \tag{2.38}$$

2.4 Analysis

Using the results of the previous section, it is possible to predict the effect of various changes to geometric and material parameters on mass transport quantities. The shape of the pressure and velocity profiles is dependent on the non-dimensional quantity m, which for many serpentine configurations falls in the range of 0.5-5. The pressure profile is shown in figure 2.5. When m is small, the pressure drops linearly because all of the flow is going through the channel. At higher values of m, the pressure profile attains curvature. It is easier to understand the curvature by looking at the velocity profile in the channel (figure 2.6). Velocity in the channel is slower near the midpoint; thus, the rate of pressure loss is also lower near the midpoint. Likewise, pressure drops faster near the corners because the magnitude of velocity in the channel is higher there (this cannot be seen in figure 2.6 because velocity is non-dimensionalized). The average velocity in the GDL is plotted in figure 2.7. When the pressure drop is linear (low m), the average velocity into the GDL is also linear. As one would expect, the velocity in the GDL, $v(x)$, is greatest at $x = 0$ because that is the point where viscous pressure loss associated with flow through the channel is highest. One interesting observation about flow through the

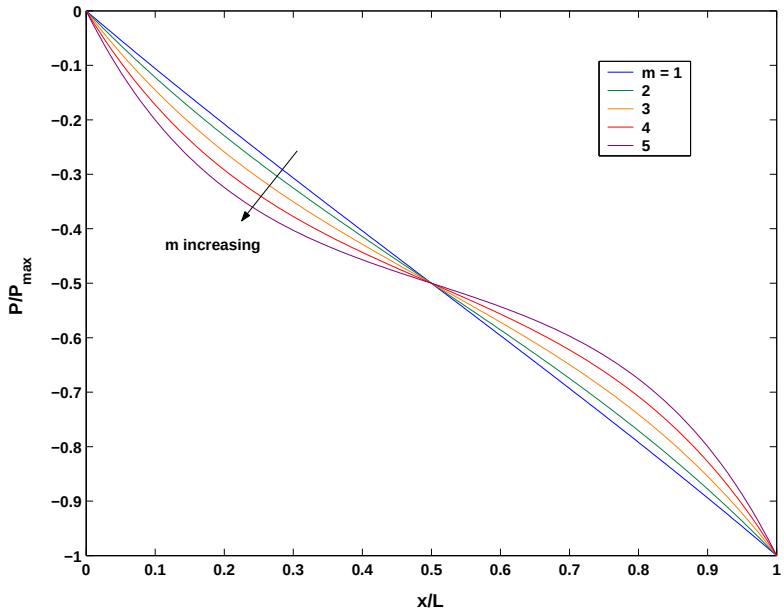

Figure 2.5: Non-dimensionalized pressure drop along the channel (from equation 2.35).

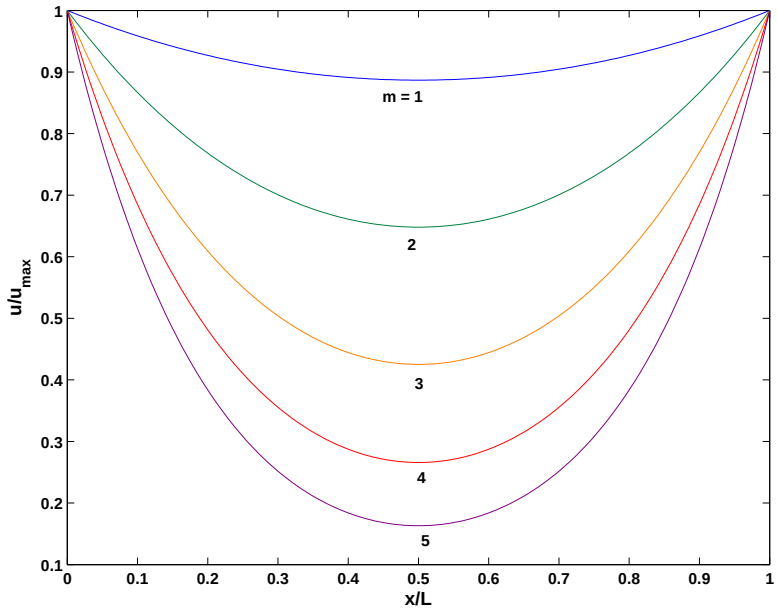

Figure 2.6: Non-dimensionalized velocity along the channel (from equation 2.36).

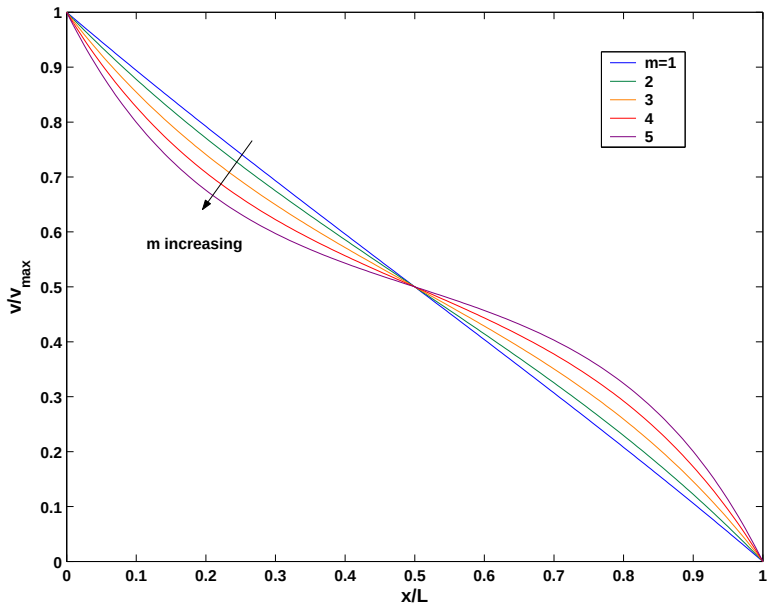

Figure 2.7: Non-dimensionalized velocity through the GDL (from equation 2.38).

GDL is that the channel-length-averaged velocity into the GDL is a constant for all values of m.

A particular quantity of interest is the amount of flow which penetrates into the land during each pass. Using the velocity profiles computed in the previous section, the ratio of fluid going around the corner of the serpentine to the flow through the GDL is

$$\frac{Q_{corner}}{Q_{gdl}} = \frac{u(x=0)A_c}{t\int_0^L v(x)dx} = \frac{2}{m\tanh\left(\frac{m}{2}\right)} \tag{2.39}$$

And the ratio of flow going around the corner to the total flow is

$$\frac{Q_{corner}}{Q_{total}} = \frac{Q_{corner}}{Q_{corner}+Q_{gdl}} = \frac{2}{m\tanh\left(\frac{m}{2}\right)+2} \tag{2.40}$$

Given the large number of dimensionless parameters which prescribe the geometric and material properties of the serpentine network, it is striking to notice the ratio $\frac{Q_{corner}}{Q_{total}}$ is only a function of one combined dimensionless parameter, m. Shown in figure 2.8 is the ratio $\frac{Q_{corner}}{Q_{total}}$ is plotted against the dimensionless parameter m. For small values of m, practically all of the flow travels around the corner of the flow channel. Near $m = 1$, the flow around the corner quickly begins to decline, and for m greater than about 2, the majority of flow through the cell travels through the GDL. Interestingly, the range of m for currently employed cells can be calculated to be somewhere between $0.5 < m < 5$. Thus, current fuel cells can vary quite widely in the amount of reactant convectively penetrating into the GDL. In one of the most commonly employed serpentine networks, the channel cross-section is square; then m from equation 2.22 takes the form

$$m = \frac{2L}{w^2}\sqrt{\frac{tk_{gdl}}{f}} \tag{2.41}$$

From this equation it is clear that m is most sensitive to changes in the channel width, w. However, increasing m by decreasing w is not always preferable as large

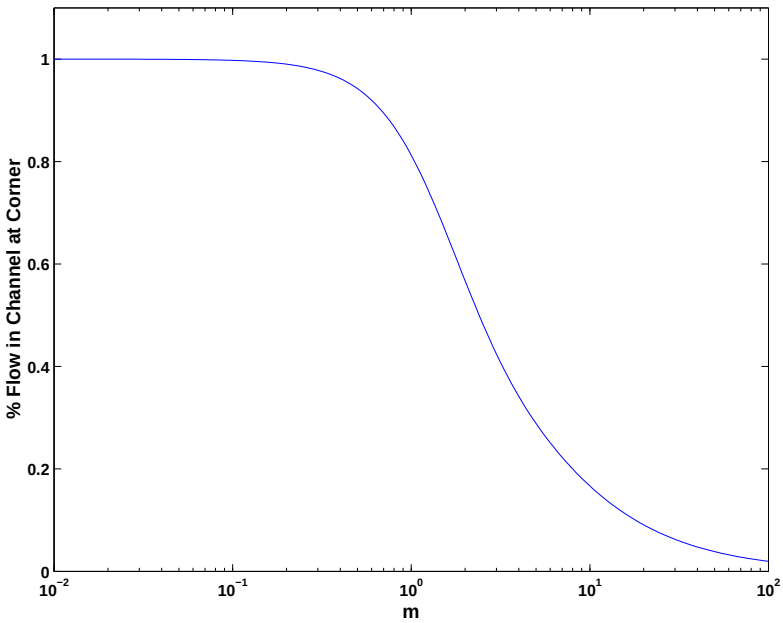

Figure 2.8: The fraction of the total flow which goes around the corner plotted against the non-dimensional parameter m defined in equation 2.22. The remainder of the flow penetrates into the GDL

pressure drops can be incurred. Another way to achieve a higher value of m is by changing the length of the channel, L. To understand why this can be a superior way of increasing convection under the lands, consider the following example.

A typical small fuel cell (say $10\,\mathrm{cm}^2$ area) with a square cross-sectional channel geometry would likely have parameters $L = 3.1\,\mathrm{cm}$, $w = 1\,\mathrm{mm}$, $b = 1\,\mathrm{mm}$, $t = 300\,\mu\mathrm{m}$, and $k_{gdl} = 1 \times 10^{-11}\,\mathrm{m}^2$. From equation 2.41, it is calculated that $m \approx 0.6$ and subsequently that only about 8% of flow travels through the GDL on each pass. However, if the area of the cell is held constant at $10\,\mathrm{cm}^2$ and the channel length is increased to 10cm (that is, the active area is made a 10 cm x 1 cm rectangle), then $m \approx 1.9$ and subsequently 41% of flow travels into the GDL on each pass. Although the channel length for each pass is increased, the total length of the serpentine channel remains the same because the active cell area was maintained. Thus, no penalty due to pressure drop is incurred; meanwhile, flow to the GDL is increased substantially.

While little experimental work is available to verify the model, a recent computational study [20] provides an excellent point for comparison. The study considers a full three dimensional treatment of convection through a unit cell of a serpentine network with a range of Reynolds number between 100-400. In order to model the interaction of the GDL with the flow channel, the study employs a modified version of the Navier-Stokes equations which uses a momentum source term consistent with Darcy's Law; this technique is commonly applied throughout the fuel cell literature. Figures 2.9 and 2.10 compare computational solutions from [20] with the analytical solution from the current study. Figure 2.9 examines the percentage of flow moving around the corner at Re=100 for two different channel lengths. This ratio is independent of Reynolds number for the analytic solution, which was derived assuming low Reynolds number. However, the figure shows that the analytic solution and computational solutions are in good agreement despite being applied at relatively

high Reynolds number. The analytic solution slightly under-predicts the pressure drop across the land and thus overpredicts the flow through the GDL; by removing assumption 2.7, the agreement can be improved. Figure 2.10 shows the anticipated pressure drop over two lengths of the serpentine for the same set of conditions. Again, analytic predictions agree very well with the computation under the caveat that the plotted analytic curve deviates slightly due to assumption 2.7.

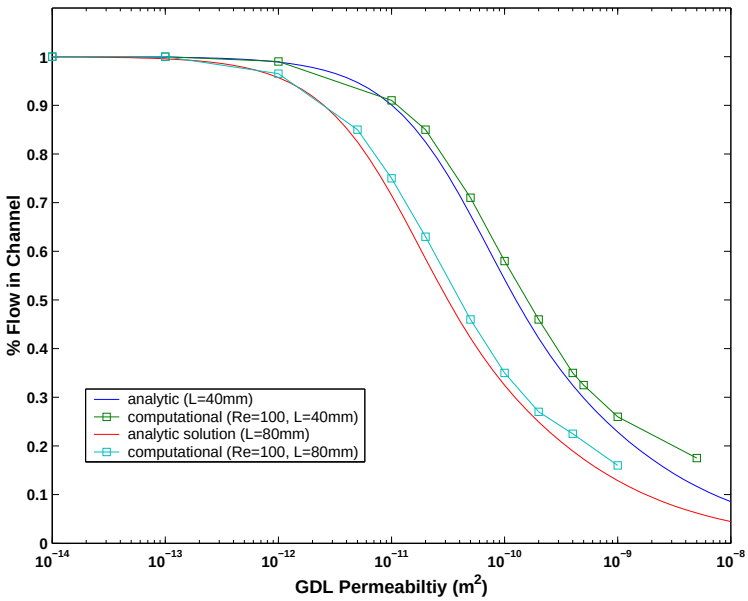

Figure 2.9: The fraction of the total flow which goes around the corner for various values of the in-plane permeability k_i and channel lengths L. Computational results reproduced from [20].

While it has been shown that proper choice of the dimensionless parameter m can increase the percentage of the flow traveling under the lands, it is not clear how this parameter relates to fuel cell performance. In fact, a more important number is the Peclét number, a relative comparison between the speed of convection and diffusion. Here the Peclét number will be defined in such a way as to show the

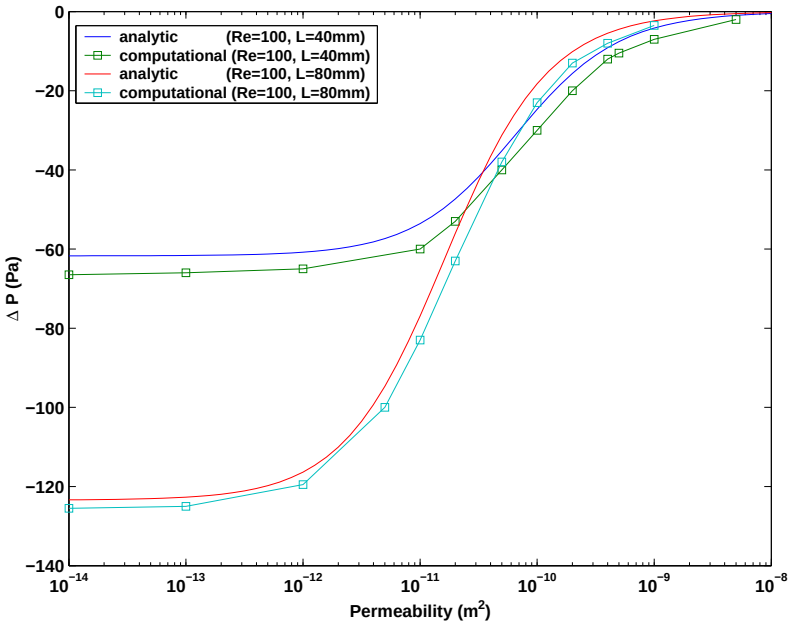

Figure 2.10: The pressure drop over a unit cell for various values of the in-plane permeability k_i and channel length L for $Re = 100$. Computational results reproduced from [20].

relative importance of convection underneath the lands in the in-plane direction and will be denoted $Pe_{\parallel}$. Then

$$Pe_{\parallel} \equiv \frac{v(x)b}{\varepsilon D} \tag{2.42}$$

where ε is the porosity of the GDL; inclusion of this term is justified because the actual fluid velocity is always higher than the artificial velocity. However, for most current gas diffusion media, porosities are relatively high (60%-90%) meaning that the artificial and actual velocities are close to one another.

As discussed in a previous section, if convection can be made to be the dominant mechanism of mass transport in a fuel cell, then reactant concentration in the gas diffusion layer and likely the catalyst layer can be raised to a level near that in the channel which will improve cell performance. Also, if convection is the primary mechanism of transport at high current densities, then diffusion-limited mass transport can be subsided. Furthermore, channel bypass can provide an escape mechanism for water vapor produced at the catalyst layer although, since the binary diffusion coefficient of water vapor in air is more than twice that of oxygen in air, large velocities are required to achieve convective dominance for water removal. Using equation 2.38, the Peclét number can be found to be

$$Pe_{\parallel} = \frac{2}{\varepsilon}\frac{k_{\text{eff}}}{k_c}\frac{L}{\ell_c}\frac{\tanh\left(\frac{m}{2}\right)}{m}\left(1 - \frac{\sinh\left(m\left(\frac{x}{L} - \frac{1}{2}\right)\right)}{\sinh\left(\frac{m}{2}\right)}\right) Sc\, Re \tag{2.43}$$

where Re and Sc are the Reynolds number and Schmidt number respectively are defined as

$$Re \equiv \frac{u(x=0)\ell_c}{\nu} \quad \text{and} \quad Sc \equiv \frac{\nu}{D}$$

where ℓ_c is the width of the channel where it contacts the GDL (for a square cross-section, it was previously called w). The Reynold's number is related to the mass of

air fed into the fuel cell. For a fuel cell operated at current density i and stoichimetry λ, the Reynolds number at the corner is given by

$$Re = \frac{M_{air}\lambda i L(b+\ell_c)\ell_c N}{4F\mu\gamma_{O_2}A_c}\left(\frac{2}{m\tanh\left(\frac{m}{2}\right)+2}\right) \tag{2.44}$$

where M_{air} is the molar mass of air and γ_{O_2} is the mole fraction of oxygen in air. For fuel cells employing square active areas, the number of channels N is approximately $N = L/(b+\ell_c)$. For analysis purposes, it is convenient to average the Peclét number along the length of the channel. Then,

$$Pe_{\parallel,avg} = \frac{2}{\varepsilon}\frac{k_i}{k_c}\frac{L}{\ell_c}\frac{\tanh\left(\frac{m}{2}\right)}{m}Sc\,Re \tag{2.45}$$

Unlike the ratio Q_{corner}/Q_{total}, the Peclét number depends on many parameters. In order to understand the relative importance of convection in current fuel cells, consider changes made to only three variables, the GDL in-plane permeability k_{eff}, the channel length L, and the thickness of the GDL t, while holding all other parameters constant(see table 2.1). This treatment assumes that the active area and the channel cross-section are square. Figures 2.11-2.13 show contours of Peclét number over a range of channel length and GDL permeability at particular values of GDL thickness. The jaggedness of the contours is not an artifact, but rather a result of setting the number of channels, $N = L/(b+\ell_c)$; N is rounded to achieve discrete values, thus the jaggedness.

The most striking feature of figures 2.11-2.13 is that the Peclét numbers are in the intermediate range. This means that at a particular cell size, choice of GDL can make a difference in terms of the primary mass transport mechanism. Experimental data presented in the current work and elsewhere in the literature, shows that in-plane permeability for commercially available GDL materials can take on a wide range of values (5×10^{-13} m^2 – 5×10^{-11} m^2). Using a gas diffusion layer at the upper end of that range, the results indicate that any cell with active area larger than 15 cm^2 will be dominated by convection. In contrast, diffusion layers at

Parameter	Value	Unit
ε	0.8	
ℓ_c	1	mm
μ	2.0e-5	Pa s
b	1	mm
λ	2	
i	1	A/cm^2
D	3.2e-5	m^2/s
ρ_{air}	1.2	kg/m^3

Table 2.1: Parameters used to generate figures 2.11-2.13

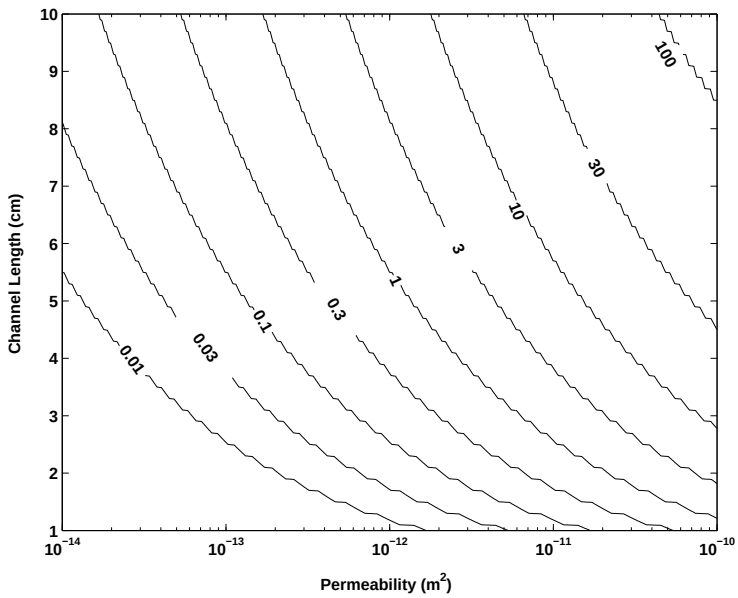

Figure 2.11: Peclét number as a function of channel length and GDL permeability for $t = 100\,\mu$m. For other parameter values see table 2.1.

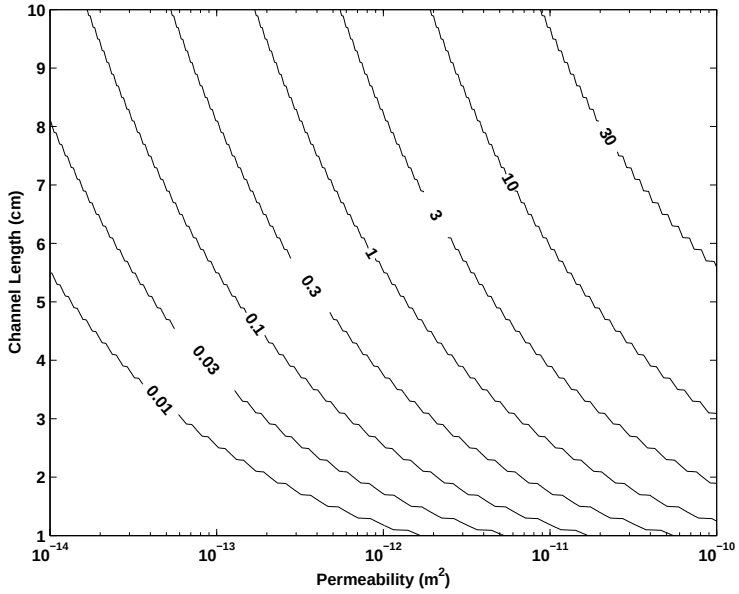

Figure 2.12: Peclét number as a function of channel length and GDL permeability for $t = 200\,\mu$m. For other parameter values see table 2.1.

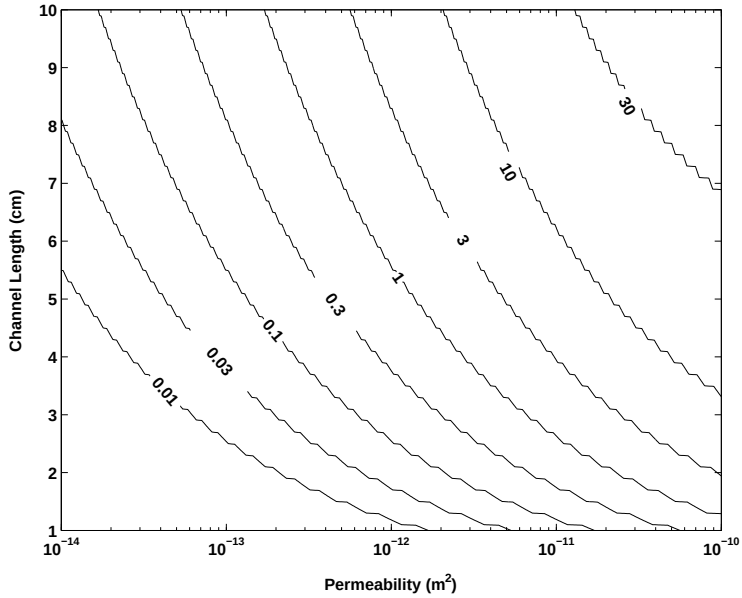

Figure 2.13: Peclét number as a function of channel length and GDL permeability for $t = 300\,\mu$m. For other parameter values see table 2.1.

the lower end of the range will not achieve convective dominance for any realistic cell size. Thus in-plane permeability is a important parameter governing fuel cell operation and proper gas diffusion layers should be chosen accordingly.

A second important result is that the Peclét number is insensitive to the choice of GDL thickness over the range of typical use. Despite a 300% change in GDL thickness between figures 2.11 and 2.13, the Peclét number changes only a few percent. This has important implications for fuel cells since reducing the thickness of the GDL can reduce material cost, stack volume, and the ohmic overpotential.

2.5 Conclusions

It has been shown that a relatively simple model can capture the physics of channel bypass in single serpentine flow field and admits a closed form solution. This model can be used to predict the relative influence of convection for a wide variety of cell design and operating parameters. It is found that the choice of GDL in-plane permeability can be a major factor in the encouragement of channel bypass driven convection. GDL thickness is found to have little impact on the relative influence of convection. It is suggested that by using rectangular cell active areas (longer channels, less passes), more channel bypass can be achieved with no additional pumping requirements.

Chapter 3

MEASURING CONVECTIVE FLOW IN FUEL CELLS USING PARTICLE IMAGE VELOCIMETRY

3.1 Introduction

Particle Image Velocimetry (PIV) is a technique used to obtain instantaneous 2D velocity fields. This is in contrast to techniques such as laser Doppler anemometry and hot wire anemometry, which have high temporal resolution but are point-wise and thus have low spatial resolution. The operating principle of PIV is as follows. A fluid is seeded with particles which are small enough to closely follow the streamlines of the flow. Then an illuminating source (typically a laser) emits two pulses of light which casts two images of the particles onto a recording media (typically a CCD camera). Because of the time delay between pulses, particles in the second image are displaced slightly from the first. A process known as interrogation is used to quantify the velocity field from the two images. To accomplish this, the two images are broken into many sub-regions known as interrogation spots which each contain small clusters of particles. Software is used to compute a discrete spatial cross-correlation between particles within the interrogation region; the point of maximum cross-correlation determines the approximate x and y displacements of the particles [21]. Using sub-pixel interpolation, the displacement can be measured to within 0.1-0.2 pixels [23]. Knowledge of the time delay between illuminating pulses allows a velocity vector to be obtained in each interrogation region, allowing one to construct the entire 2D velocity field.

3.2 PIV as a Fuel Cell Diagnostic

One of the active areas of fuel cell research is the development of visualization techniques. Several groups have developed transparent fuel cells primarily designed to qualitatively observe the transport of liquid water in hydrogen fuel cells ([26],[31]) and carbon dioxide bubbles in direct methanol fuel cells ([32],[1],[2],[12]). One quantitative technique that has recently been developed is thermal neutron imaging([9],[10],[19]). This technique operates by directing a collimated neutron beam into a hydrogen fuel cell; the neutron beam is scattered by liquid water by an amount related to the thickness of water. By scanning the entire fuel cell, a 2D map can be created of water content in the cell. While thermal neutron imaging is effective for observing liquid water movement at rate up to 30 frames/s with resolution of about 100 μm, it provides no information about the reactant flow within the cell. Another limitation caused by the fact that it provides integrated information about water formation is that it cannot determine the plane of existence of the water.

Particle Image Velocimetry can be used to provide information about velocity fields within the flow channels of fuel cells. Such information could prove useful in understanding the role of convection in fuel cells as well as to validate numerical models. A recent study has used PIV to investigate secondary flow at U-turns similar to those at the corners of serpentine fuel cells [13]. A dimensionally scaled model was constructed from acrylic in which two channels were connected by squared turn. PIV was able to determine that secondary flows associated with the U-turn are stable for Reynolds number less that about 400; beyond this, turbulence ensues both in the corner and downstream. It is concluded that reactant would be well mixed in the flow channel under such conditions. While this apparatus was able to model the turbulent nature of the turns of a fuel cell, it does not model any of the other aspects of convection in the fuel cell. Specifically it cannot model the channel bypass described in the previous chapter, because it did not include a porous layer

underneath the acrylic flow channel.

In an ideal situation, micro-PIV could be used to measure velocity fields in active fuel cells. However, this ideal scenario can be difficult to achieve in practice for several reasons. One of the basic requirements of PIV is that the apparatus be transparent which is an obvious difficultly of an operational fuel cell because the apparatus (i.e. the representative bipolar plate) must be conductive. Since there are no materials which are simultaneously highly conductive and optically transparent, other methods of current collection are needed such as a thin layer of gold underneath the lands. A more difficult problem is that seeding particles would need to be chosen carefully so as to not interfere with fuel cell performance. Further, at high magnifications needed to resolve the flow, optical considerations such as depth of field, object distance, and creation of the light sheet become overburdening, particularly when trying to observe secondary flows. Despite the difficulties involved, microscale PIV cannot be ruled out as a tool for observing certain aspects of live fuel cells at full scale. At least one group claims to be pursuing just this [15].

However, the current study employs dimensional analysis in order to alleviate some of the issues encountered while observing live fuel cells. Since air is composed of 79% nitrogen, for the purposes of measuring convective flow in the channels it is reasonable to assume that, on the cathode side of air breathing fuel cells, reactant is not consumed and that it is incompressible. Then, observations made of a model in the absence of a chemical reaction should closely resemble the flow that is observed in an operational fuel cell. If a live fuel cell is not used, the representative flow channels, gas diffusion layer, and membrane can be made from any transparent material without consequence and the choice of fluid becomes arbitrary so long as all relevant dimensionless parameters can be matched.

3.3 Experimental Setup

An experimental apparatus was constructed to measure velocity fields representative of those in a fuel cell using PIV. A flow field was designed to model the behavior of a 15 cm^2 fuel cell operating at an equivalent current density of 4 A/cm^2; the flow field is reconfigurable, capable of operating as a parallel, serpentine, or interdigitated network. The flow channels were constructed by adhering optically clear acrylic pieces together to form five parallel channels. The four internal ribs have dimensions 360 mm x 9.5 mm x 9.5 mm. The flow channels are 9.0 mm wide and 9.5 mm tall. A buffer of 10 mm was left between the edge of each rib and the outer viewing window (see figure 3.1). To create serpentine and interdigitated flow fields from the parallel configuration, rubber plugs were cut and friction fitted into appropriate regions of the acrylic base as indicated in fig. 3.1.

In order to match the relevant dimensionless parameters of a fuel cell, care must be taken to properly scale permeability of the porous medium that lays beneath the 'bipolar plate.' Because permeability carries the units of m^2, it is necessary to scale permeability by the geometric scaling squared. Since, the geometric length scaling of the model is a factor of 10, the permeability should be scaled by a factor of 100. Experimental data presented in the current work and elsewhere in the literature, shows that in-plane permeability for commercially available GDL materials can take on a wide range of values (5×10^{-13} m^2 $- 5 \times 10^{-11}$ m^2). An isotropic frabric with e-glass fibers randomly oriented was found to be suitable, having an in-plane permeability on the order of 1×10^{-9} m^2 at a thickness of 3.2 mm, which would then represent a GDL at the upper end of the range with a thickness around 320μm. An aluminum spacer wrapped in PTFE tape was used to provide the proper thickness of the porous medium as well as to seal the model from the surroundings. A solid aluminum plate was placed under the porous medium to act as the 'impermeable' membrane. Finally, a top aluminum plate with cutouts for optical access

was fastened to the bottom plate (See figure 3.2). Ports were drilled into the acrylic to serve as the inlet and outlet for fluid flow.

A submersible pump was used to circulate water from a reservoir into the apparatus. Before returning to the reservoir, water flowrate was controlled using an acrylic flowmeter with metering valve. The region of interest was illuminated by twin Nd-YAG lasers (Continuum Surelite II), operating at 10 Hz, and providing 30 mJ per pulse (pulse duration=6 ns) at a wavelength of 532 nm. Spherical and cylindrical lenses were used to form a light sheet of appropriate thickness and intensity. Images were recorded on a CCD camera (1280 x 1020 pixel) specialized for single frame-double pulse PIV (LaVision ImagerIntense). Fluorescent particles (20-40 μm) were used to seed the flow; the particles have the unique property that they fluoresce at a wavelength higher than the incident. By using fluorescent particles in conjunction with a long wave filter, background noise can be significantly reduced while retaining high image intensity of the particles. In a further attempt to reduce background noise and increase particle correlation, a background image (200 images averaged together) was subtracted from each PIV image.

Image interrogation was performed using in-house software. An interrogation spot size of 64 x 64 pixels with a 50% overlap was chosen in order to allow sparser particle seeding which is necessary to view cross sections deep within the model.

PIV was performed on the interdigitated and serpentine flow field geometries. An important insight is that, despite the fact that the two flow fields are both meant to model behavior of fuel cells of equal area and current density, the two models should not receive the same flowrate; this is because the apparatus is not an exact geometric scaling of the prototype 15 cm^2 fuel cell. The model was only 9 cm wide with 5 channels, whereas the prototype would be about 38 cm wide with about 19 channels. Thus, the nature of each flow field must be considered. In a serpentine, the flow for the entire cell is carried primarily through the single flow channel. In

this case, the obvious matching condition is appropriate.

$$\left(\frac{\dot{m}}{\mu w}\right)_{\text{prototype}} = \left(\frac{Q_{in}}{\nu w}\right)_{\text{model,serpentine}} \tag{3.1}$$

where $\dot{m}_{\text{prototype}}$ is the air mass flux computed from the prototypes' equivalent current density and active area. However, in interdigitated flow as well as parallel flow the fluid is distributed among many channels. Then, the proper way to assure that each channel in the model experiences a similar flow to that of the prototype is to scale the model flowrate by the ratio of the actual geometric scaling to the exact (proper) geometry scaling (in this case the ratio is 9/38), so that

$$\left(\frac{\dot{m}}{\mu w}\right)_{\text{prototype}} = \left(\frac{Q_{in}}{\nu w}\right)_{\text{model,interdigitated}} \left(\frac{9}{38}\right) \tag{3.2}$$

This corrective factor would not be necessary if the model was built as an exact dimensional match. However, using this technique simplifies the manufacturing of the model considerably. Using this reasoning, inlet flowrates of 15 cm^3/s and 3.5 cm^3/s were used for the serpentine and interdigitated flow fields respectively.

A coordinate system was defined in order to describe the position of each measurement (see figure 3.2). The channels have been designated numbers, number 1 being the closest to the inlet and number 5 being closest to the outlet. The dimension z is used to describe the distance along the channel, while dimensions x and y are used to describe the width and height of each channel. Note that this coordinate system is different than the one defined in the previous chapter.

Experiments in the interdigitated configuration focus on the observation of channel-to-channel crossover. Cross-sectional images in the xy plane were taken for several values of z along channels 2 and 4 (exiting 'fingers'). Images of the yz plane were also taken in the center of all 5 channels in order to observe the primary flow near the finger edges of channels 1, 2, and 3. PIV in the single serpentine configuration was conducted along xy cross-sections of channel 3 for several values of z. Channel 3 was chosen because its flow is anticipated to be the most similar

to the spatially periodic flow encountered in the center of the prototype device. For both sets of experiments, multiple images (typically 75) were acquired and the instantaneous velocity fields obtained by interrogation were averaged in order to produce smooth plots which are representative of the bulk motion. Images acquired deep within the channels ($z \approx 20$cm) were particularly noisy because of the large number of particles and glass fibers which stood in the way; for these regions, 200 velocity fields were acquired and averaged.

Conducting 2D PIV on cross-sectional views of fuel cells presents a significant challenge because the primary flow is out-of-plane. If precautions are not taken, then particles which are in the light sheet during the first pulse will not remain for the second pulse; this would cause loss of correlation during interrogation. In order to overcome this obstacle, the current study makes use of a very thick light sheet and large f-numbers of the camera lens which promotes a large depth of field. To determine how thick of a light sheet is needed, a criteria that at least 3/4 of all particles should remain in the light sheet for good correlation was used. Then, for a light sheet of thickness δz and a through-plane velocity of $V_{\text{through-plane}}$ the maximum time interval between pulses is given by

$$\delta t = \frac{1}{4} \frac{\delta z}{V_{\text{through-plane}}} \tag{3.3}$$

In order to achieve a value of δt which was high enough to observe large particle displacements, a suitable value of δz was found to be approximately 3 mm. In order to observe particles over such a large depth, special lens consideration were made. The depth-of-field for a single lens and iris focusing on an image plane is given by

$$\delta z = 4(1 + M^{-1})^2 (f^{\#})^2 \lambda \tag{3.4}$$

where M is the lens magnification and λ is the scattered wavelength. Then since $\lambda \approx 532$nm and $M \approx \frac{2}{3}$ in the current experiment $f^{\#} \geq 16$ must be used. Using such a large depth-of-field has at least two disadvantages. First, raising the f-number

means that less of the available light is being collected; thus, it is necessary to operate at high laser powers for sufficient lighting. Second and perhaps more important is that large f-numbers increase the diffraction limited spot size according to

$$d_{spot} = 2.44(1 + M)(f^{\#})\lambda \tag{3.5}$$

Using $f^{\#} = 16$, the diffraction limited spot size at the lowest suitable f-number is found to be 34μm which is quite large compared to the seeding particles (20-40μm). Thus, the f-number should not be raised any more than necessary.

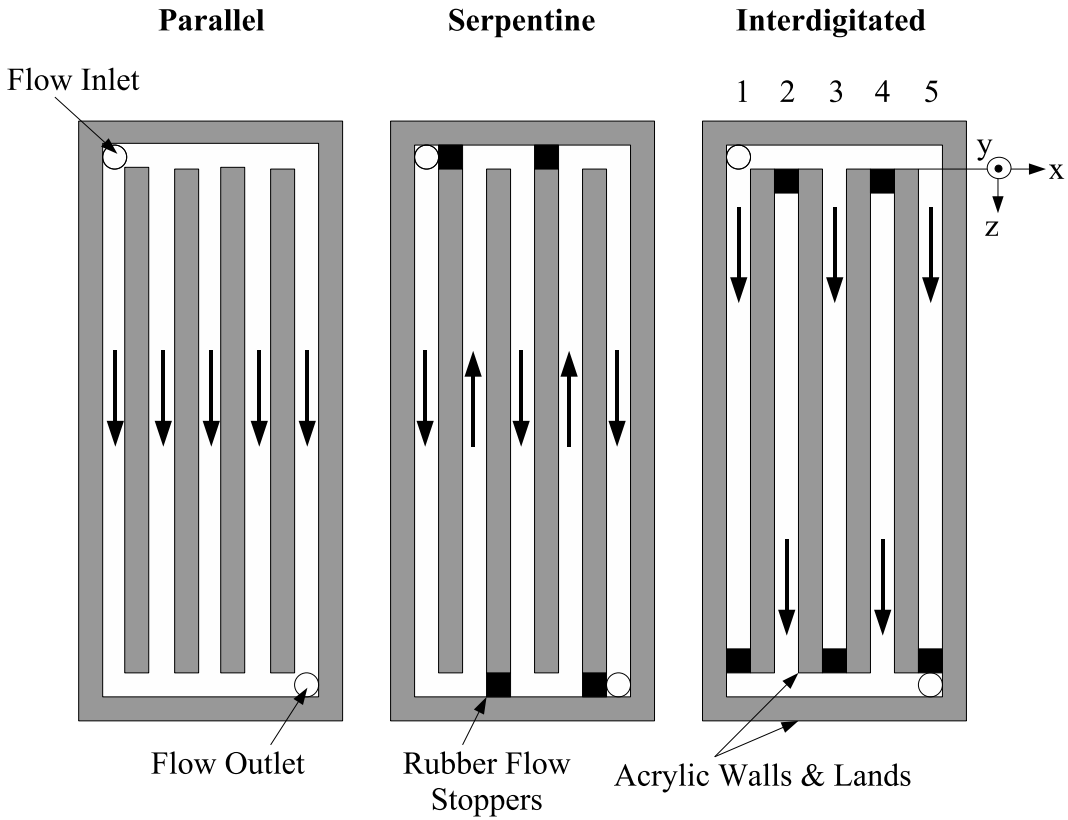

Figure 3.1: Diagram of the flow field constructions used for experiments. Note that the coordinate system is different than the one used in a previous chapter.

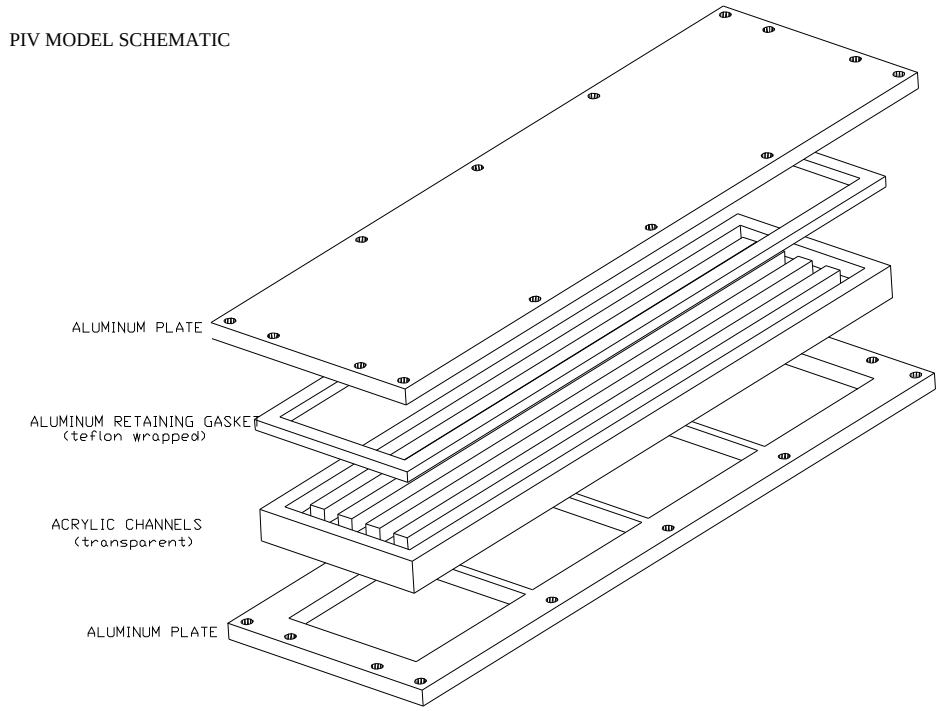

Figure 3.2: Exploded assembly of the flow field constructions used in experiments. For illustrative purposes, it is shown upside-down.

3.4 Results

3.4.1 Interdigitated PIV

Due to the symmetry of the interdigitated flow field used, it was anticipated that velocity fields in the fingers of channel 2 and 4 should resemble a mirror image of one another at equal values of z. Figures 3.3-3.5, show a comparison of channels 2 and 4 for three different values of z. At $z = 34$cm, a clear infusion of fluid from the porous medium is visible. However, flow in channel 2 and 4 are not mirror images of one another as expected. Flow entering channel 2 from the right side is substantially less than flow entering channel 4 from the left. This is a trend repeated at $z = 30$cm

and $z = 25$cm. One possible explanation for this is that the porous medium could have a local variation in thickness or in permeability; this is particularly possible because the randomly oriented glass fiber has visible regions which have sparser fiber volume fraction than others. In retrospect, a sparsely woven cloth may have been a wiser choice for the porous medium. However, the random glass fiber mat is very similar in pore structure to carbon fiber paper and non-woven gas diffusion layers, so perhaps the unevenness is truly representative of the physics in a fuel cell. In the absence of velocity field data from full size fuel cells, that is difficult to determine.

Velocity fields taken in the yz plane near the end of the inlet fingers are shown in figure 3.6. A comparison of the three return channels (1,3,5) shows that the velocity fields are all very similar. It is interesting that the velocity magnitudes near the edge of the fingers are still quite large compared to the cross-sectional components.

Velocity fields in the yz plane of the return channels are shown in figure 3.7. Since at this point of the cell, the two channels carry almost all of the return flow, the primary velocity is quite high near the center of the channel (about 30mm/s). It has a near parabolic profile, such as that expected in a fully developed pipe flow. If we compare velocities in the primary direction with the secondary velocities, it is seen that the secondary velocity moves at only about 1% the speed of primary flow! This makes measurement of the secondary velocities quite difficult as mentioned in the previous section.

3.4.2 Single Serpentine PIV

Velocity fields were determined in the xy plane of the center channel (channel 3) in a serpentine arrangement at various z locations. Figure 3.8 shows the flow just after the 180˙ turn; as expected, large secondary flows are present, likely corresponding to the Dean's flow around the corner. The secondary Dean's vortices quickly diminish; figure 3.9 shows the flow just 5 cm from the turn. Flow appears to

emerge from the left side ($x \approx 0$) of the porous medium and submerge on the right ($x \approx 1$); this is a clear view of channel bypass. This is somewhat surprising, given that the analytic formulation in the previous section predicts that little channel bypass should be occurring on the left side ($x \approx 0$) of the flow at this z location. Similarly, flow into the porous medium at large values of z was expected to be small on the right side ($x \approx 1$). Again, this is not observed; flow submergence at $x \approx 1$ is relatively even over all the z locations. However, one aspect of the observations is consistent with the model; in general, flow emerging from the bottom-left side of the velocity fields in figures 3.8-3.15 appears to become more intense at larger values of z. Figure 3.16 shows the development of the flow along the z coordinate. While the analytic model in the previous section claims an anti-symmetry should exist in the velocity field in the z coordinate, a relationship between the flow at $z = z^*$ and $z = L - z^*$ does not appear to exist. There are two major possibilities why this could happen. First, the analytic model does not include inertial effects. Perhaps the inertia from the entering jet at $x \approx 0$ or the secondary flows from the 180˙ turn drives the fluid back into the porous layer at $x \approx 1$; For example, the inertially driven vorticies at the turn appear to drive fluid into the GDL ($z = 1$). As with the interdigitated PIV results, perhaps local variations in the permeability of the porous medium are to blame for the unevenness in flow velocities along the length of the channel. However, local variations in permeability still cannot explain why flow would travel into the porous medium near the turns, where according to the model, no pressure difference should exist. For this reason, the phenomena might warrant further research.

3.5 Conclusions

Particle Image Velocimetry was used to observed the velocity fields in representative test sections of a interdigitated and serpentine fuel cell. Using ex-situ

methods, it was shown that it is possible observe secondary flows with primary-to-secondary velocity ratios approaching 100-to-1. Channel bypass in both configurations was clearly observed. Local variation in permeability of the porous medium appears to have an important effect on the evenness of velocity fields in the models. It is suggested to use woven type porous materials in the future to isolate the effects of localized permeability. Inertial effects such as Deans vorticies may also influence convection into the GDL.

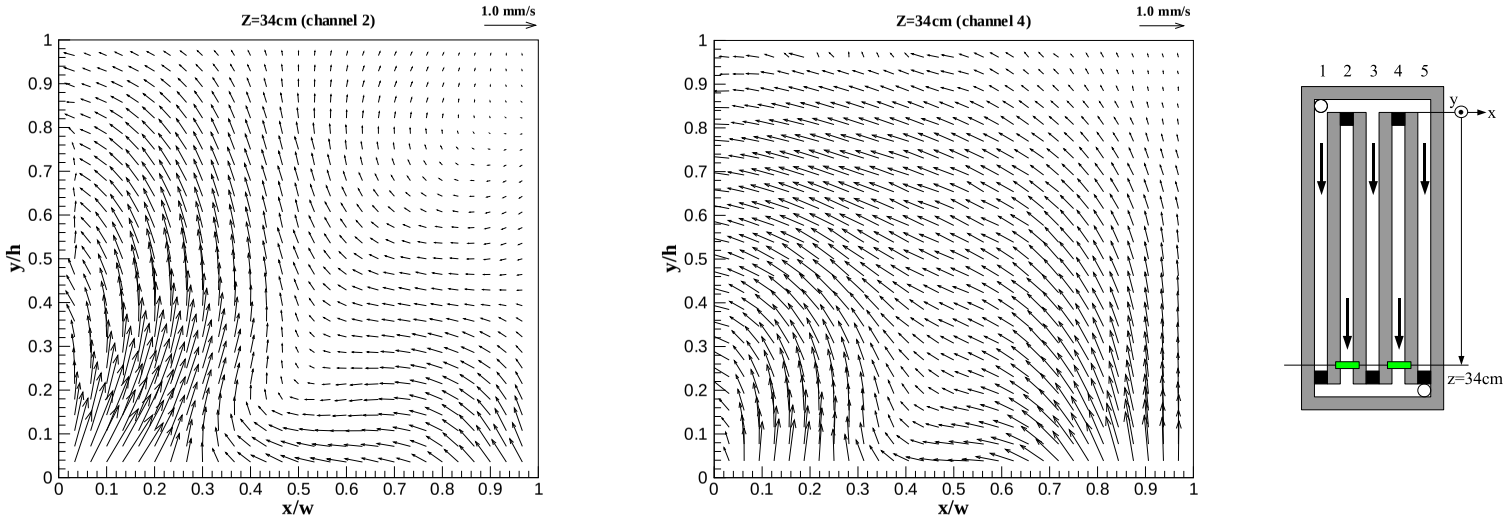

Figure 3.3: Cross-sectional PIV of return fingers in an interdigitated flow field ($z = 34$cm)

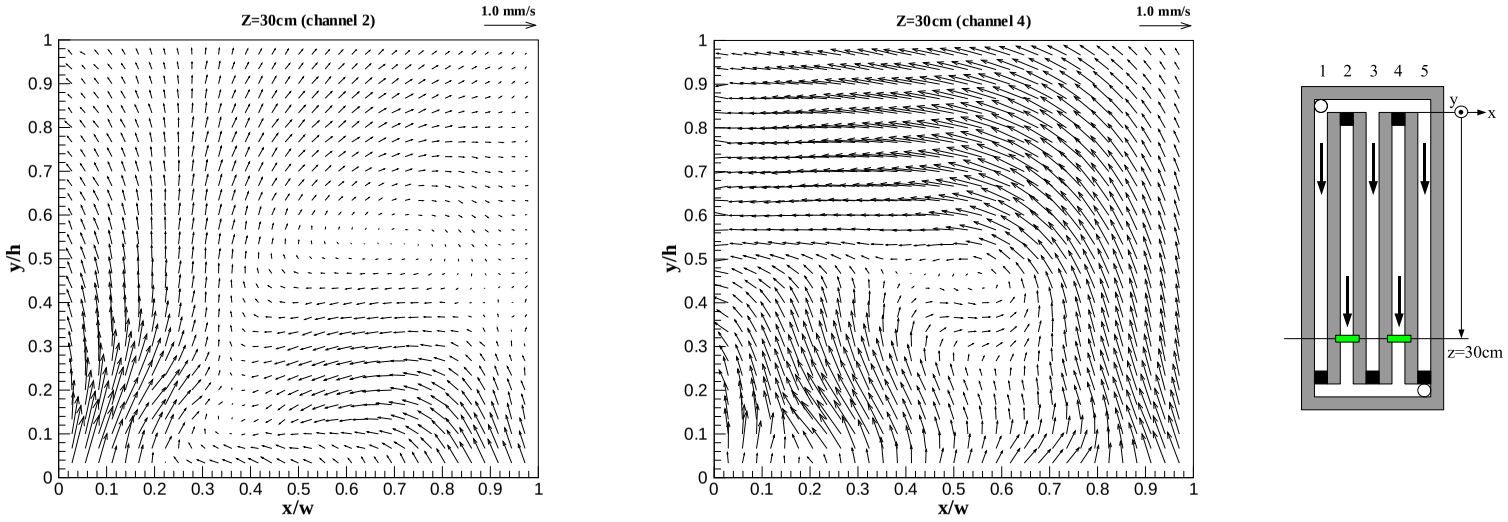

Figure 3.4: Cross-sectional PIV of return fingers in an interdigitated flow field ($z = 30$cm)

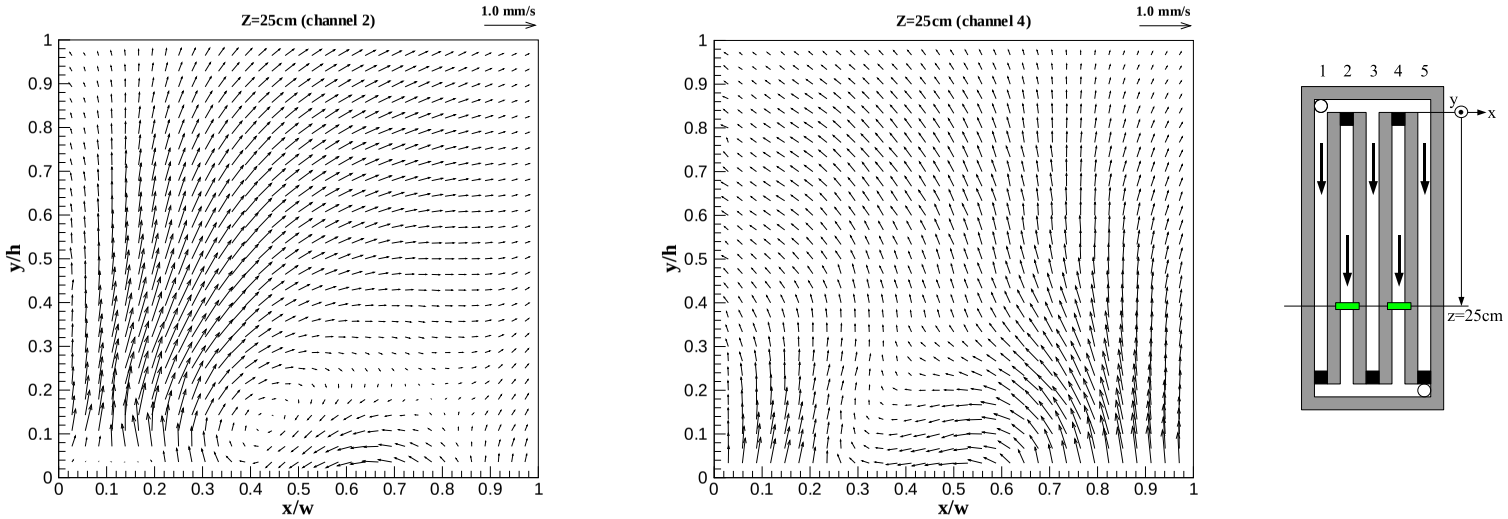

Figure 3.5: Cross-sectional PIV of return fingers in an interdigitated flow field ($z = 25$cm). In channel 2, a fiber has protruded into the channel leading to self-correlation along the bottom.

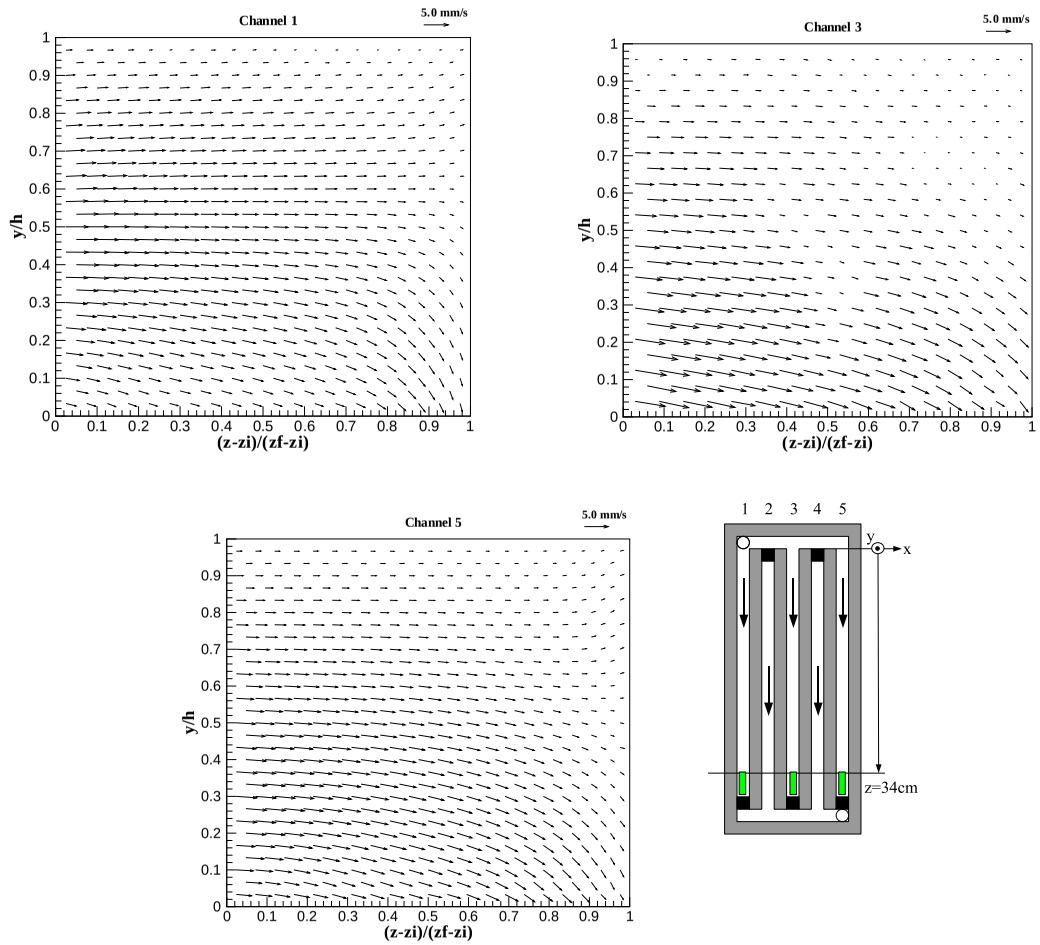

Figure 3.6: Longitudinal PIV of inlet fingers of the interdigitated flow field. $z_i = 34$cm and $z_f = 35$cm. For illustrative purposes only 1 out of every 2 velocity vectors is shown. In channel 3, smudges on the test section have resulted in self-correlation near the center of the frame.

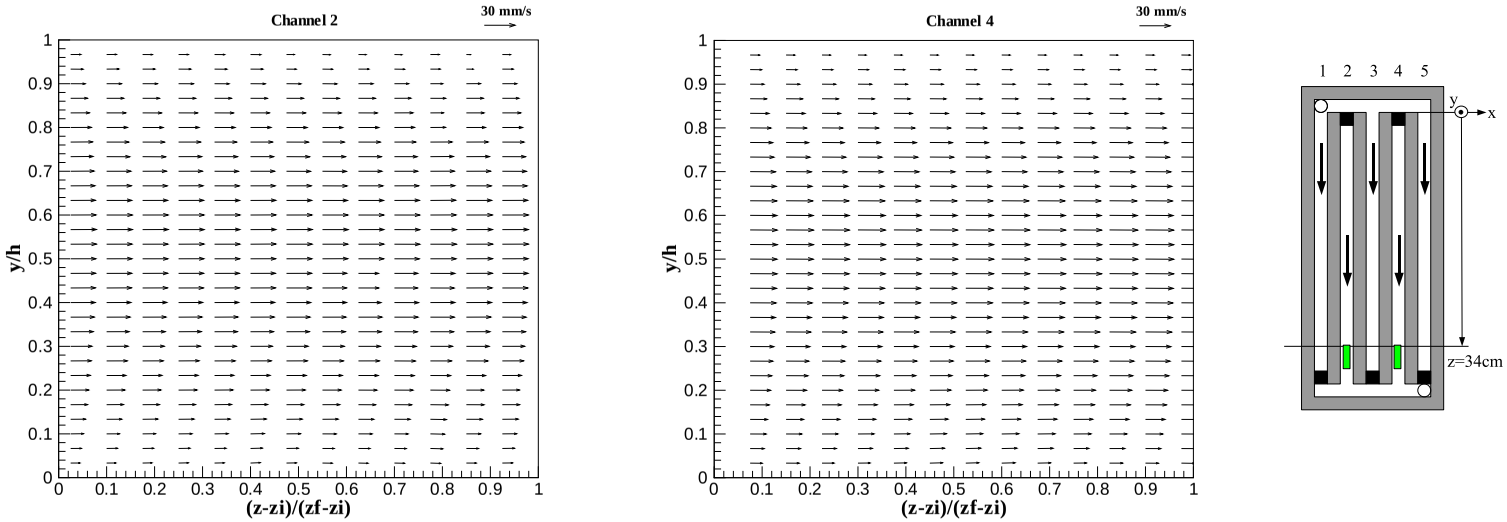

Figure 3.7: Longitudinal PIV of return fingers of the interdigitated flow field. $z_i = 34$cm and $z_f = 35$cm. For illustrative purposes only 1 out of every 3 velocity vectors is shown.

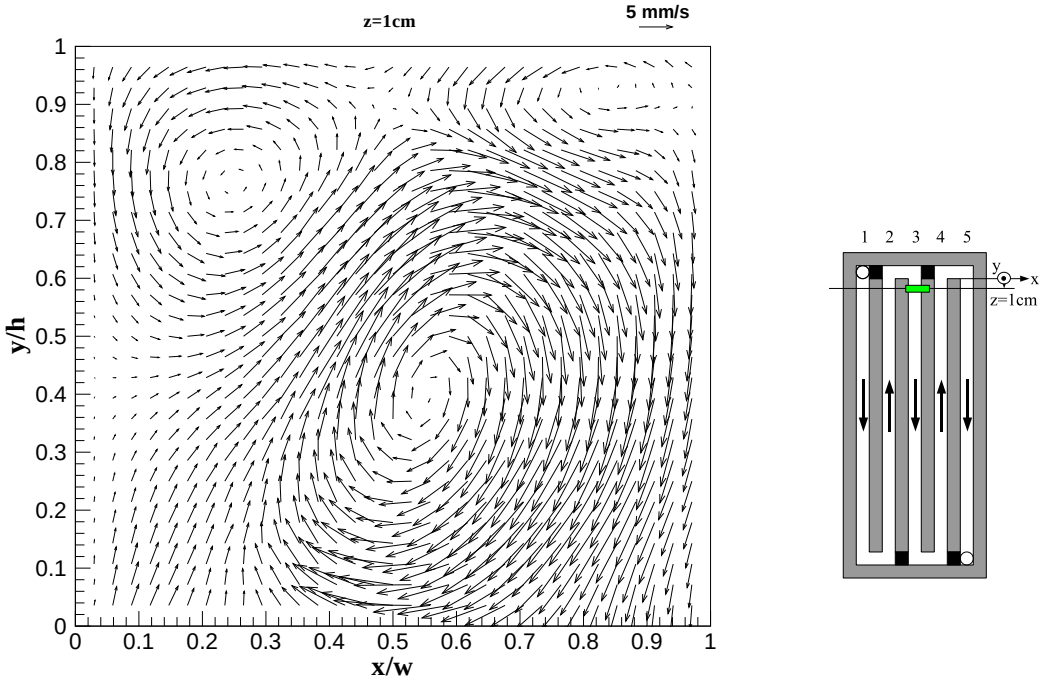

Figure 3.8: Time averaged velocity field at z=1 cm (channel 3) in the serpentine flow field configuration. Significant secondary flows are present due to the proximity of the turn.

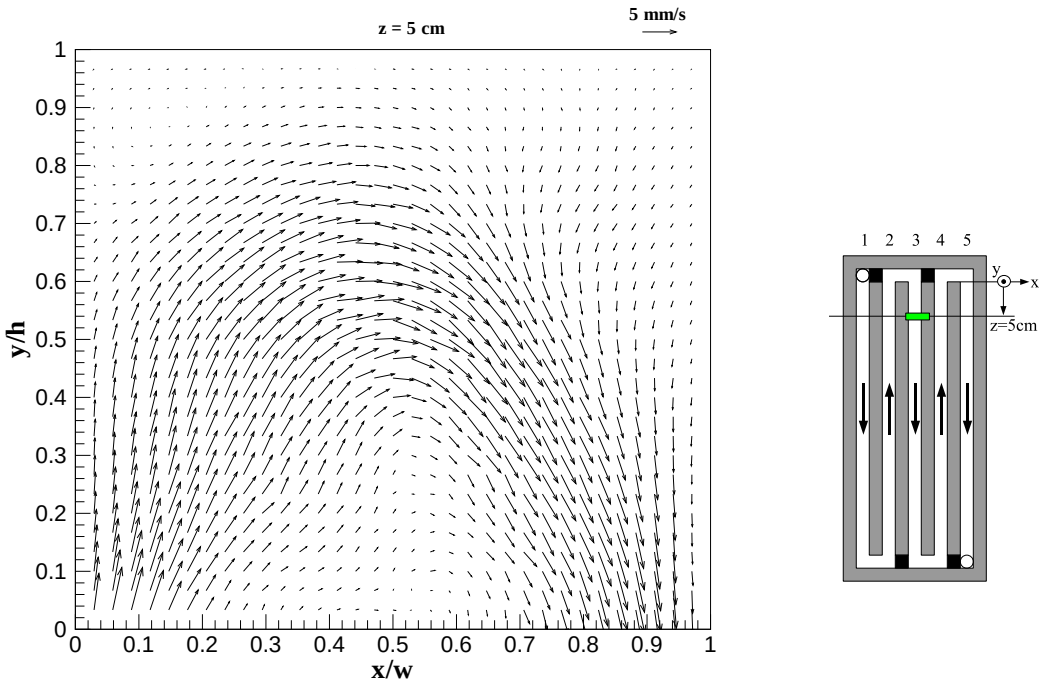

Figure 3.9: Time averaged velocity field at z=5 cm (channel 3) in the serpentine flow field configuration.

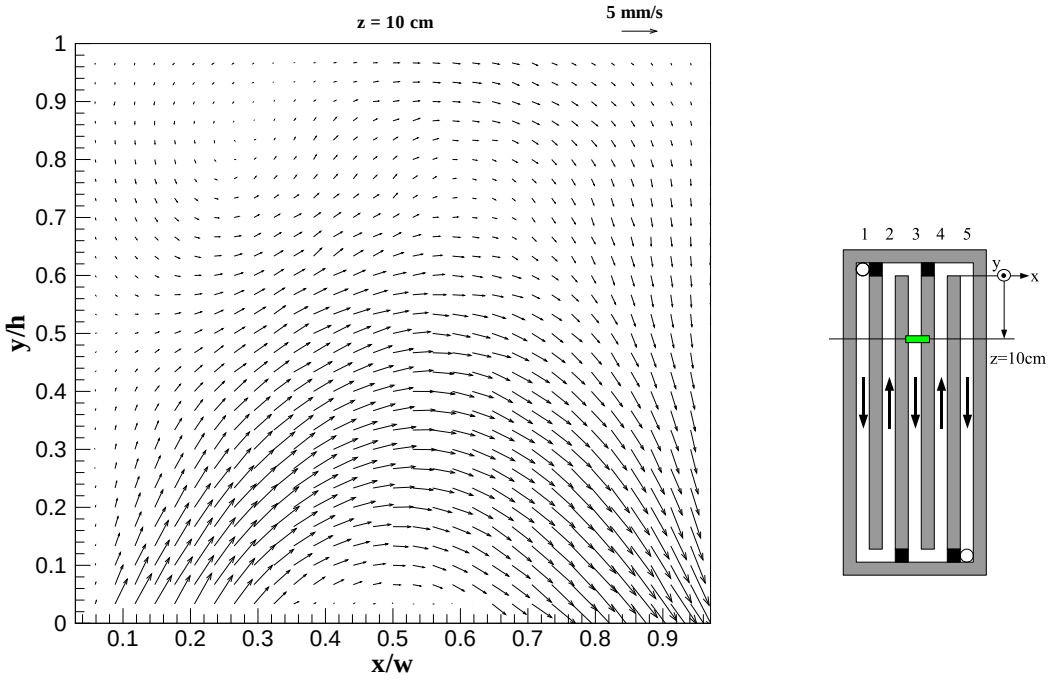

Figure 3.10: Time averaged velocity field at z=10 cm (channel 3) in the serpentine flow field configuration.

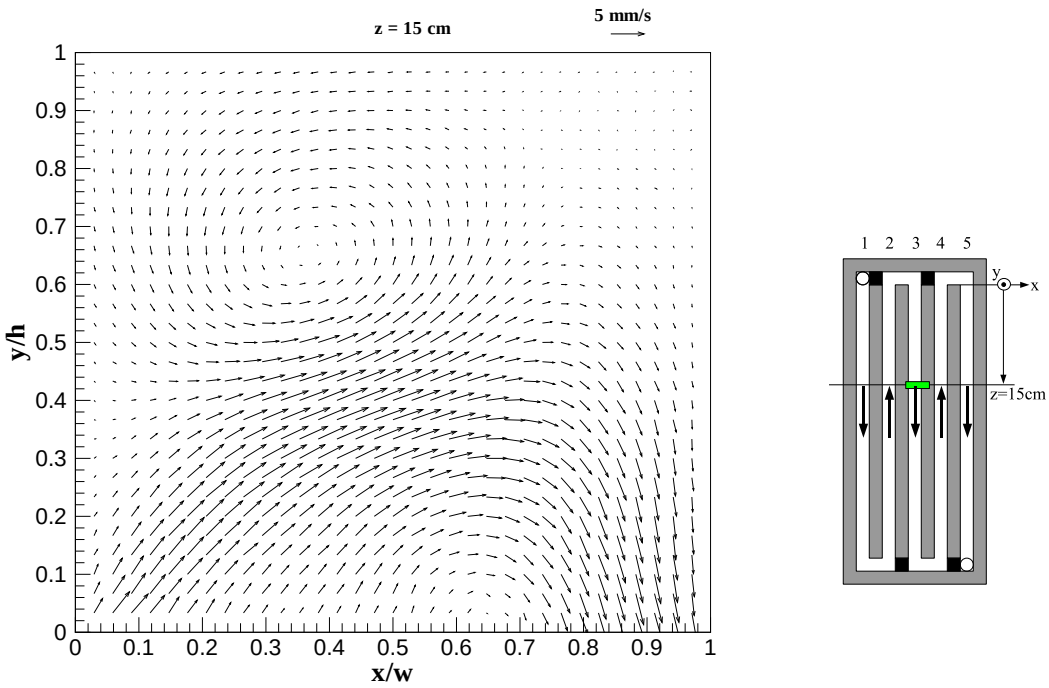

Figure 3.11: Time averaged velocity field at z=15 cm (channel 3) in the serpentine flow field configuration.

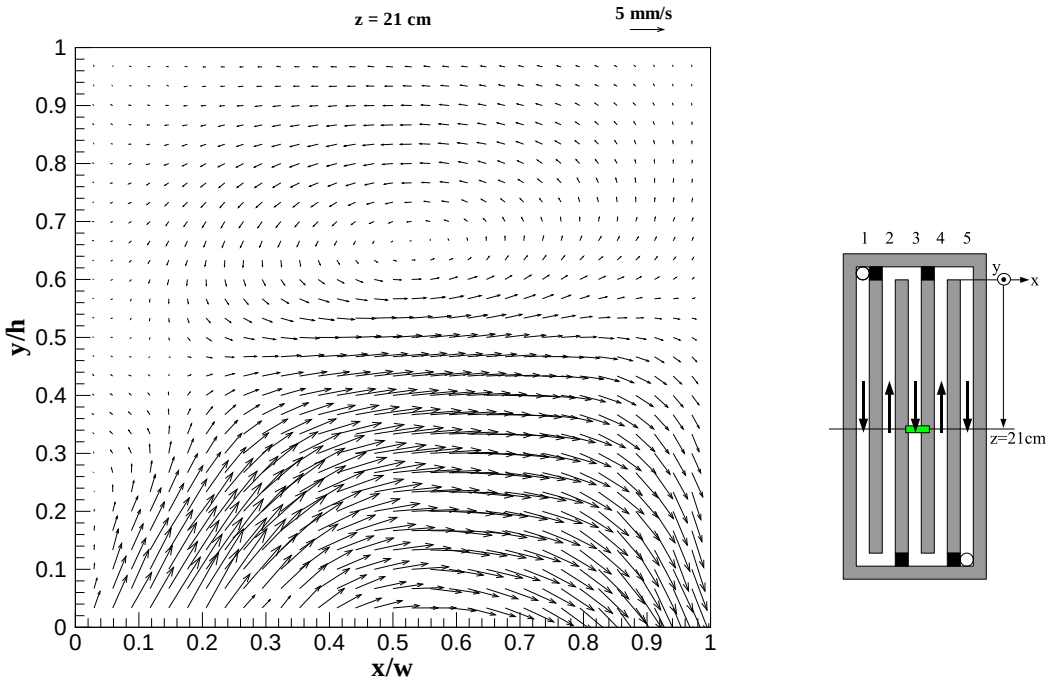

Figure 3.12: Time averaged velocity field at z=21 cm (channel 3) in the serpentine flow field configuration.

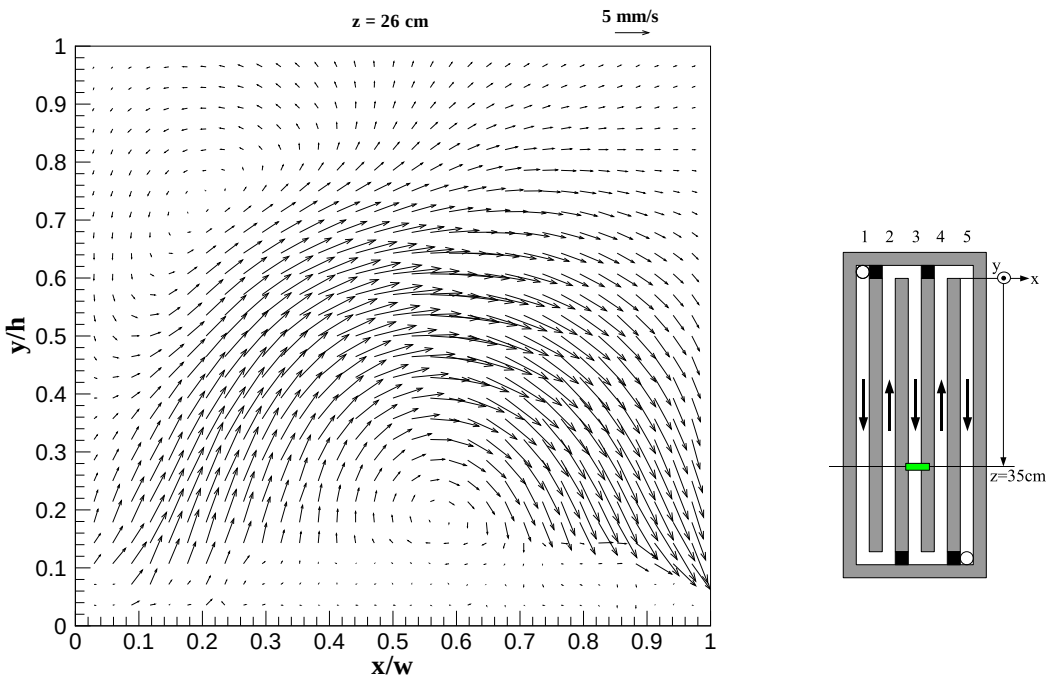

Figure 3.13: Time averaged velocity field at z=26 cm (channel 3) in the serpentine flow field configuration. A significant number of fibers have protruded into the channel leading to self-correlation along the bottom.

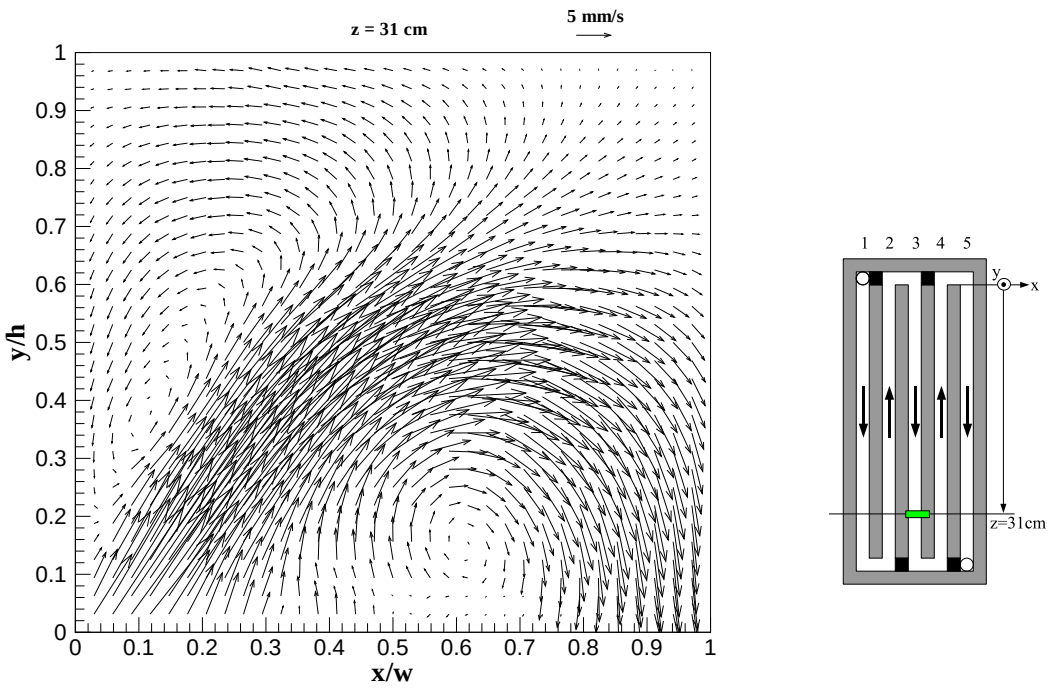

Figure 3.14: Time averaged velocity field at z=31 cm (channel 3) in the serpentine flow field configuration.

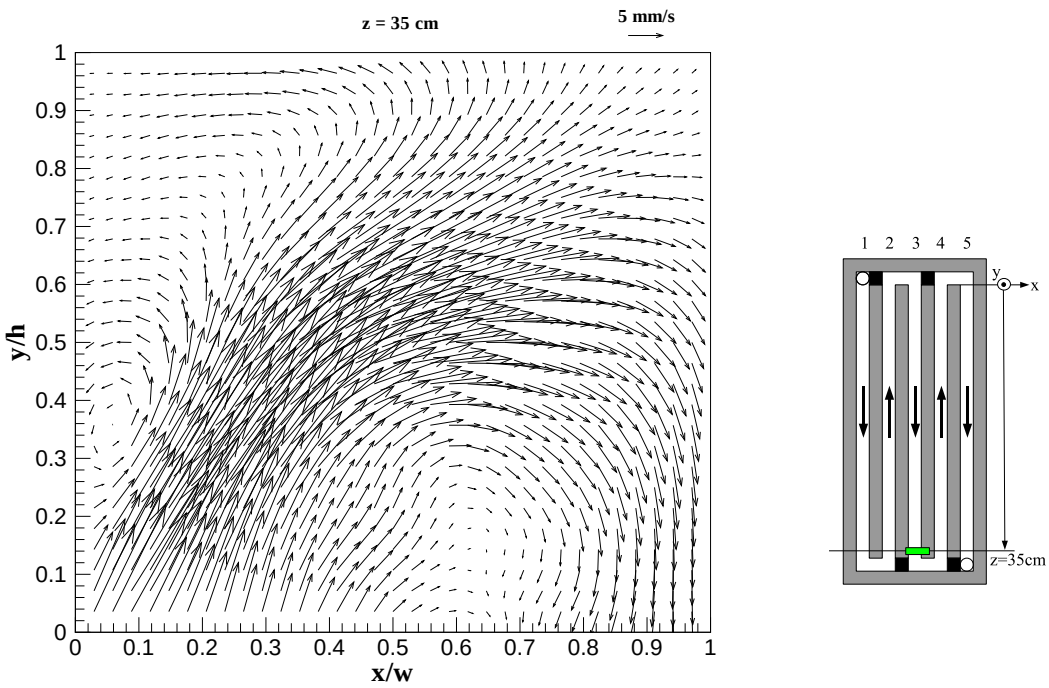

Figure 3.15: Time averaged velocity field at z=35 cm (channel 3) in the serpentine flow field configuration.

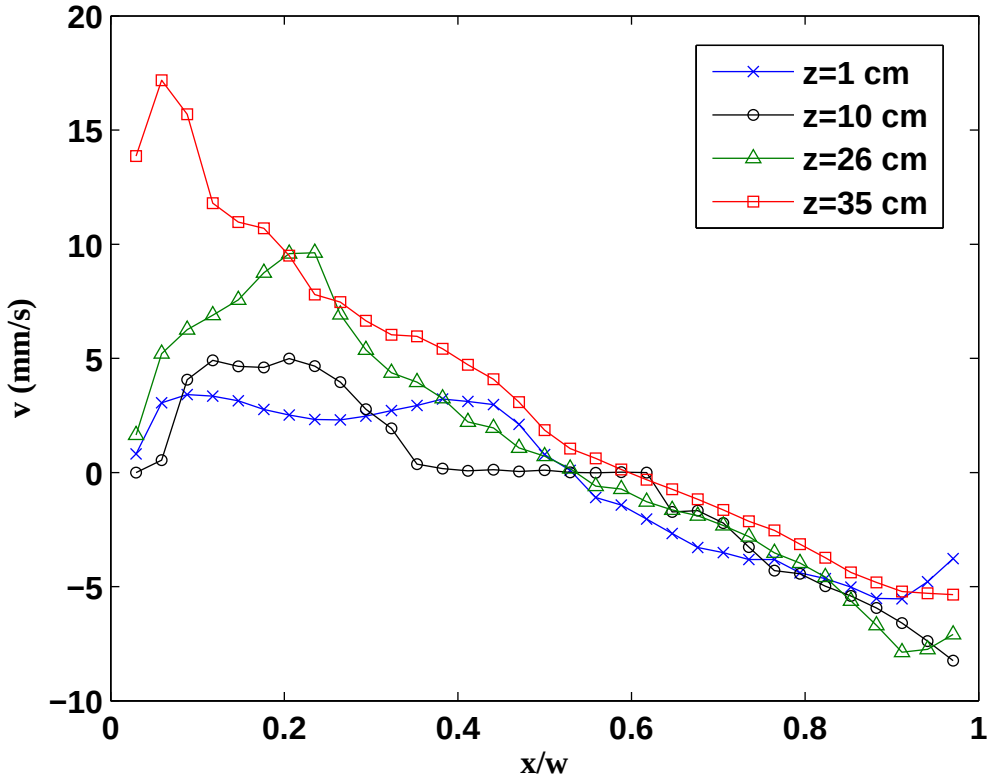

Figure 3.16: Vertical velocity at the y-location closest to the porous media ($y = 0$) for various values of z in the middle channel of the serpentine configuration (channel 3). The values at the $z = 26$cm location have been taken along the line $\frac{y}{h} = 0.14$ instead because of the fibers which protruded into the channel.

Chapter 4

EXPERIMENTAL DETERMINATION OF IN-PLANE PERMEABILITY OF GAS DIFFUSION MEDIA

4.1 Motivation

The gas diffusion layer serves five key purposes [14]: mechanical support, electronic conductivity, heat removal, reactant access to the catalyst layers, and product removal from it. The latter three functions can be improved by increasing convective mass transport into and out of the gas diffusion layer. In general, convection can be improved through porous media by increasing the material property of permeability. Improved performance due to increased convection is well documented in interdigitated flow fields ([27],[17],[6],[7],[25]). For interdigitated flow fields, GDL permeability does not heavily affect the operation of a cell operated at a given stoichiometry as the total reactant penetration is the same regardless of permeability (100%). Instead, GDL permeability reduces the required pumping power needed to achieve a given stoichiometry. In serpentine flow fields, the role of the relative influence of GDL permeability and convection in general has been debated throughout the literature. Mench [16] concluded based on 3D computer modeling that reactant bypass could adversely affect cell performance by starving regions further along the channel. This is in contrast to 2D modeling work which predicts that channel bypass will positively affect performance [25]. Experimental data shows that limiting current density is both independent of diffusion and strongly dependent on through-plane permeability [30]. The analytic treatment in the current work as well as a

computational treatment [20] predict that the in-plane permeability should have a strong effect on mass transport in serpentine fuel cells. In a recent review on gas diffusion layer characterization, Mathias [14] also points to in-plane permeability as the relevant parameter in fuel cell performance, citing diffusion as the dominant mechanism for through-plane transport and thus that through-plane permeability should not be important.

Aside from the conclusions of Mench, there are other reasons to justify using a gas diffusion layer which operates at low permeability. While three of the five key roles of the gas diffusion layer are improved with increased convection, low electrical contact resistivity apparently requires a trade-off; Electronic resisitivity is reduced substantially by increasing compressive force whereas permeability (and therefore reactant and product mass transport) is reduced by it [29]. Polarization curves obtained at various levels of compression confirm that this is an important optimization process in fuel cell operation [11].

Thus, there is a need in the fuel cell community for methods to measure gas diffusion layer permeability and various compressive loadings. Methods are widely available to measure the through-plane permeability. Indeed, many GDL manufacturers provide information related to the through-plane permeability as a material specification. A variety of methods can be used to obtain through plane permeability; One common method, which provides a so-called Gurley parameter, involves measuring the time taken for a known volume of gas to pass through a sample of known area under constant pressure; this is useful for low permeability diffusion layers such as those containing a microporous layer [14]. Other techniques include using the Darcy's Law to calculate permeability from the 'dry curve' of a capillary flow porometer [8]; this has the advantage that pore size and structure as well as the free surface area can also be obtained as part of a single experiment. A device using a similar technique, but not equipped for porometry was presented recently

by Bluemle [4] along with experimental data for several ETEK series gas diffusion electrodes. An interesting aspect of this work is that the Darcy-Forchheimer convection model was used so that the experiment yielded both the viscous (Darcy) permeability and the inertial permeability. However, what little through-plane convection does exist in a fuel cell is viscously dominated, thus it is difficult to see the utility of the inertial permeability term. One significant limitation of all the current through-plane permeability techniques is that they cannot operate while compressing the GDL; thus, the decrease in permeability associated with realistic compressive loadings is neglected.

Fewer techniques have been used to characterize the in-plane permeability of the gas diffusion layer. Mathias [14] describes a method in which two flow channels can be used to determine the in-plane permeability by measuring the flowrate-pressure relationship. While this technique is valid in principle, achieving the necessary sealing can be difficult in practice because of the rectangular geometry. An easier method is to measure the flowrate-pressure relationship through an annulus of GDL material; By clamping the upper and lower edge of the annulus with a sufficiently flat and smooth plate, proper sealing can be achieved. This method was recently used by Bluemle [4]. In a series of experiments, gas diffusion layers compressed to measured force loadings by an Instron machine and they're permeabilities determined by passing compressed air through an annulus and measuring pressure again flowrate. Assuming incompressibility of the gas and using Darcy's Law, permeability was obtained from a least-squares fit of the data.

Several improvements can be made over the existing technologies which may allow in-plane permeability to be measured more accurately and with increased flexibility. One of the difficulties in measuring in-plane permeability is the small (and occasionally non-uniform) thickness of the gas diffusion layer; some GDLs are as small as 100 μm thick. Thus, if the annulus idea is used to measure permeability

of a single GDL, in order to achieve a proper seal the clamping plate should have a dimensional flatness tolerance of only a few microns, which is well beyond the capability of most common machining methods. It is suggested that by increasing the effective thickness of the GDL by stacking multiple layers during experiments, the dimensional tolerances of the clamping plates can be relaxed. For example, by stacking 8 layers of a 100 μm material the total thickness becomes 800 μm for which a realistic machining tolerance of 25 μm can be used to follow the contours of the GDL to within about 3% of its thickness.

One issue that arises when trying to measure the permeability of the gas diffusion layer is that the mean pore size can be large for the macroporous layer (about 30 μm-100 μm). If one is to measure the permeability using a technique such as that described by Mathias [14], it is questionable as to whether there are a sufficient number of pores to define an average quantity such as permeability (this is also true for fuel cells in general). In order to ensure that enough pores are present to achieve a well-averaged permeability, an annulus of 15 cm OD x 9 cm ID was used.

4.2 Measurement Technique

A radial flow apparatus (Fig. 4.1) was fabricated to test samples of GDL for in-plane permeability at various levels of compressive strain. The samples consisted of annuli of material 15 cm OD x 9 cm ID stacked to a height of approximately 1 mm with each layer of material separated by thin layer of brass shim (51 μm each); this was done to avoid nesting effects between stacked layers. Shim stock was used to control the total thickness of the compressed stack. For gas permeability experiments, compressed air (0-550 kPa) was forced through the sample, passed from the outlet to a variable area rotameter for flowrate measurement, and subsequently released into the atmosphere. In liquid permeability experiments, a pressurized tank (0-200 kPa) forced water though the sample and was collected in a graduated

cylinder at the outlet. In the case of gas permeability, pressure was measured using gauges at both the inlet and the outlet as rotometers were found to account for a significant pressure loss. For the case of liquid permeability, pressure was measured by a gauge on the inlet only and assumed to be atmospheric pressure at the outlet.

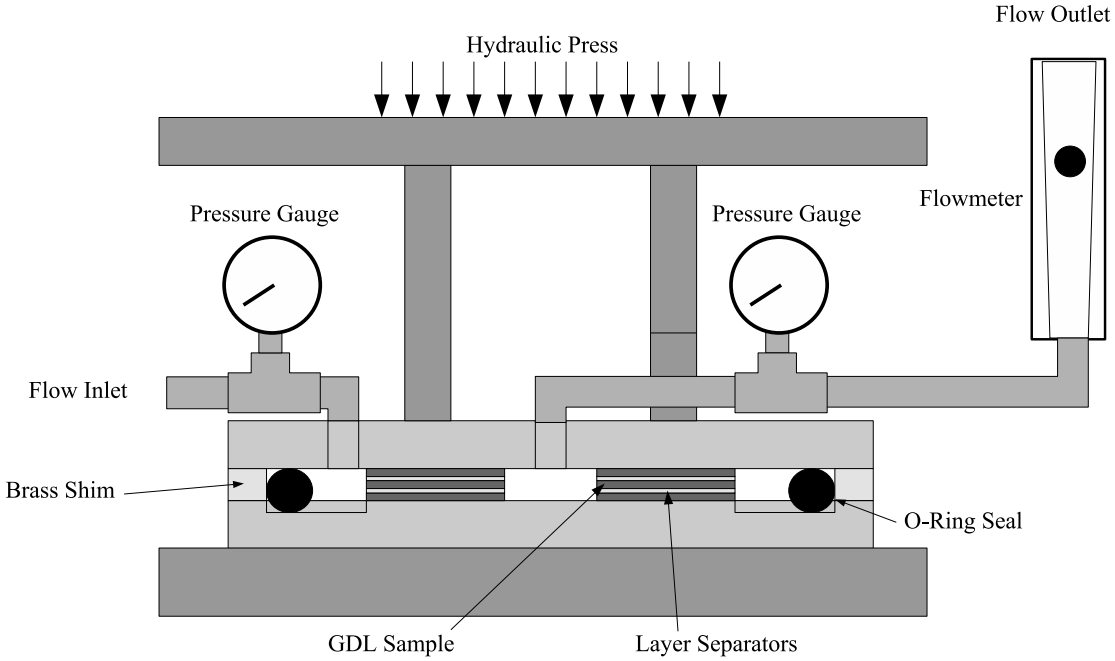

Figure 4.1: Diagram of Permeability Testing Apparatus

The measurement technique is to record pressure at approximately 10 different levels of flowrate. The collected data can be used to determine permeability once a model is established. In this case, we use Darcy's Law under the assumption that in-plane permeability is homogenous and isotropic. In radial coordinates,

$$\bar{v} = -\frac{k_i}{\mu}\frac{dp}{dr} \tag{4.1}$$

Mass conservation requires that in the annulus

$$0 = \frac{d}{dr}\left(\rho \bar{v} A\right) \tag{4.2}$$

The density term has been left in the equation because we intend to allow for compressibility effects which may become important if pressure variations are large. If equations 4.1 and 4.2 are used in conjunction with the ideal gas law, then

$$0 = \frac{d}{dr}\left(\frac{p}{RT}\frac{k_d}{\mu}\frac{dp}{dr}2\pi r h\right) \tag{4.3}$$

$$0 = \frac{d}{dr}\left(rp\frac{dp}{dr}\right) \tag{4.4}$$

Where 4.4 assumes $T \neq f(r)$ (i.e. isothermal expansion). The boundary conditions are $p(r_{in}) = p_{in}$ and $p(r_{out}) = p_{out}$, where pressure is measured in the absolute sense. If equation 4.4 is then integrated, then

$$C = rp\frac{dp}{dr} \tag{4.5}$$

Integrating a second time

$$C = \frac{p_{out}^2 - p_{in}^2}{2\ln(r_{out}/rin)}) \tag{4.6}$$

Then

$$\frac{dp}{dr} = \frac{1}{rp}\frac{p_{out}^2 - p_{in}^2}{2\ln(r_{out}/rin)}) \tag{4.7}$$

Now, we wish to related the outlet flowrate to the pressure. So

$$\begin{aligned} Q_{out} &= \left(\bar{v}A\right)_{r_{out}} \\ &= \left(-\frac{k_d}{\mu}\frac{dp}{dr}\right)_{r_{out}} 2\pi r_{out} h \\ &= \frac{\pi k_i h}{\mu \ln(r_{out}/rin)}\frac{p_{in}^2 - p_{out}^2}{p_{out}} \end{aligned} \tag{4.8}$$

Then equation 4.8 gives the relationship between pressure and flowrate. This is the equation that is used to calculate gas permeability. It should be noted when

the difference between the inlet and outlet pressures is low, this equation can be linearized in p and reduces to the well known relationship

$$Q_{out} = \frac{2\pi k_i h}{\mu} (p_{in} - p_{out}) \tag{4.9}$$

which also valid for incompressible fluids. This is the equation used to calculate liquid permeability.

A method of this type can be used to calculate a material's permeability so long as wall effects are negligible. To determine if wall effects are negligible, it is useful to introduce the idea of 'permeability' between parallel discs (such as in the case of a hydrostatic bearing). The flowrate-pressure relation is well known and is given by

$$Q_{disc} = \frac{\pi h^3}{6\mu \ln(r_{out}/rin)} (p_{out} - p_{in}) \tag{4.10}$$

comparing this with the form of 4.9, it is sensible to define the permeability of parallel discs to be

$$k_{disc} = \frac{h^2}{12} \tag{4.11}$$

currently available gas diffusion layers have thicknesses in the range 100μm-500μm. Thus, corresponding range of k_{disc} is then 8×10^{-10}m^2-2×10^{-8}m^2. Since no GDL has even been reported to have a permeability on the order of 10^{-10}m^2, it is safe to assume that the wall effects are negligible and that the measured permeability is the true material permeability.

4.3 Validation

While equation 4.8 has appeared in at least one publication in relation to soil science, no known experimental validation has been done. Thus, in order to determine its validity, an experiment was conducted to verify that the permeability obtained using an incompressible fluid (water) for which the method is well known, corresponds to the permeability obtained using a compressible fluid in conjunction

with equation 4.8. A densely woven glass fabric annulus (15 cm OD x 9 cm ID) of initial thickness 600μm was compressed to 380μm and subjected to both a liquid and a gas permeability experiment. For the liquid permeability experiment, water was chosen as the fluid in order to encourage full wetting of the pores; a constant inlet gauge pressure of 180 kPa was used. The results are shown in Figs. 4.2 and 4.3.

The parabolic dependence of flowrate on pressure for compressible flow is clearly demonstrated by fig. 4.2. Note that it would not be possible to find a least-squares fit of the linear equation which would fall within the error bounds of the data points. However, if a non-linear least squares method is used to fit a curve to equation 4.8, such a curve can be obtained. It should be noted that in the current study a non-linear least squares fit was not used because the equation was parabolic, but rather because flowrate data was collected over multiple orders of magnitude by multiple flowmeters; thus, the error bounds of the data are not equal throughout the range of collection and the residual scheme of the least squares method should be modified to minimize the sum of logarithm of the residuals rather than simply the residuals themselves. Using this scheme, the gas permeability of the glass fabric was determined to be $k_i = 5.89 \times 10^{-13}$ m^2. In comparison, liquid permeability data indicated the permeability of the same sample to be $k_i = 6.02 \times 10^{-13}$ m^2. Since the difference between the two measurements is quite small, it can be concluded that equation 4.8 is valid. It should also be noted that fitting gas permeability to the incompressible equation results in a gross over-estimation of permeability; at least one paper in the literature appears to have made this oversight [4].

4.4 Measurements of GDL Permeability

Permeability was measured on three types of gas diffusion layers, each representing one of the major manufacturing techniques: woven carbon fiber (cloth),

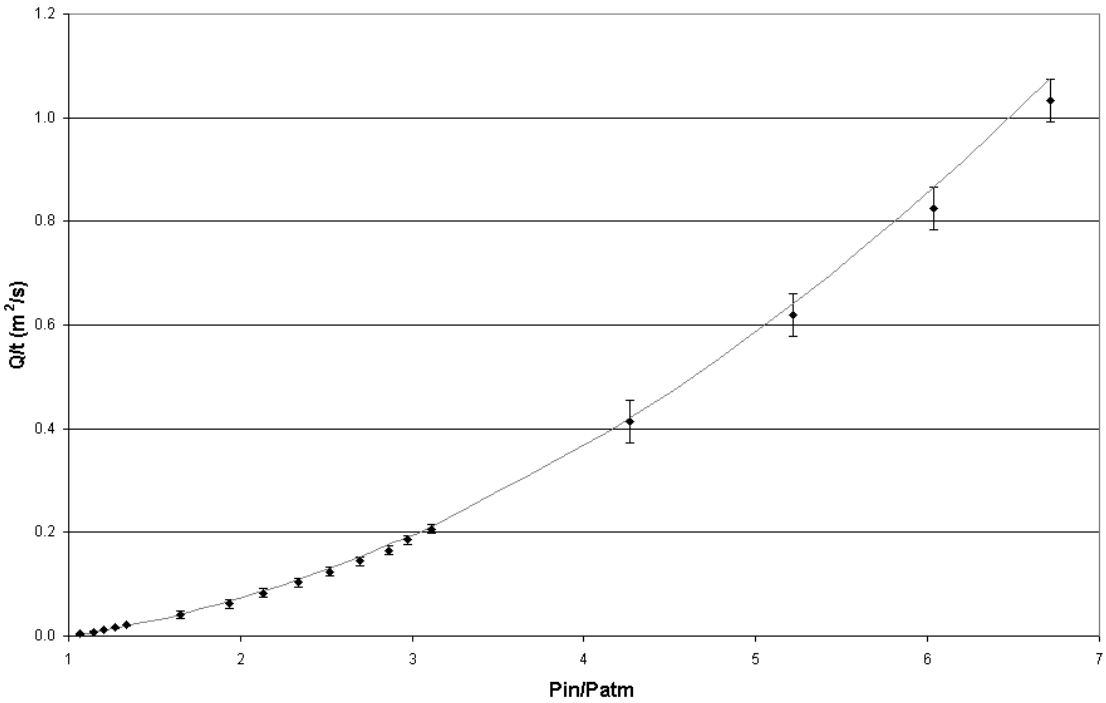

Figure 4.2: Experimental data points for air while using tightly woven glass fabric as the porous media. Solid line represents a non-linear least-squares fit of equation 4.8. Computed gas permeability $k_i = 5.89 \times 10^{-13}$ m^2

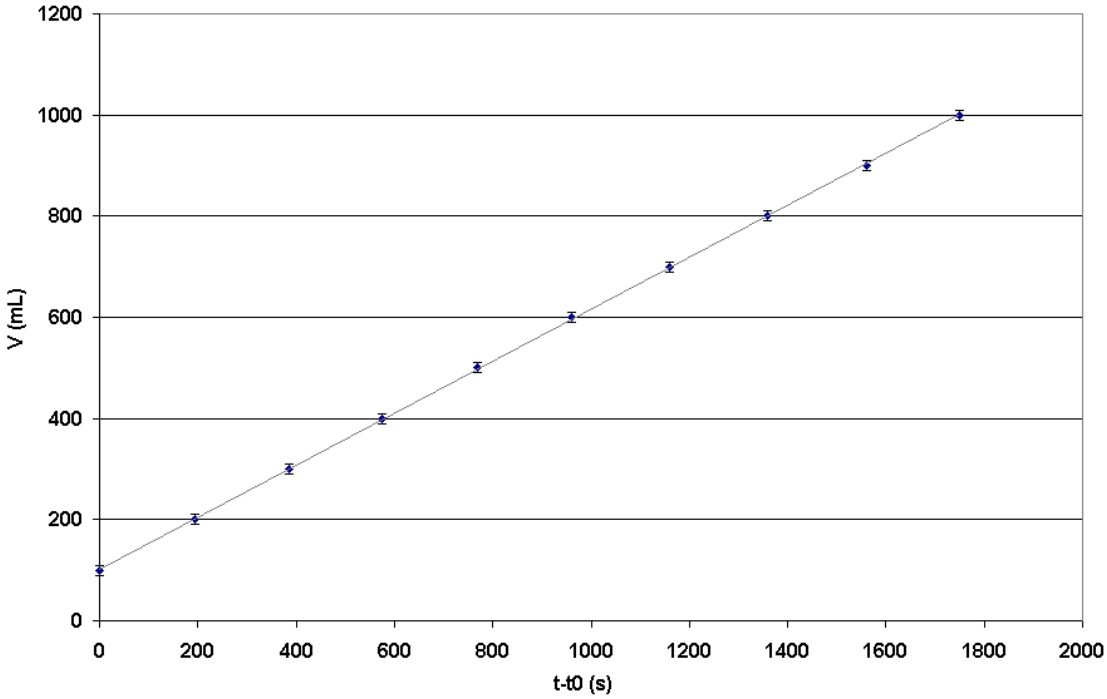

Figure 4.3: Experimental data points for water while using tightly woven glass fabric as the porous medium. Solid line represents a least-squares fit of equation 4.9. Computed liquid permeability $k_i = 6.02 \times 10^{-13}$ m^2

Sample	Initial Thickness, h_o	Thickness Fractions (%), $h/h_o \times 100$
Avcarb 1071-HBC	335μm	94%, 90%, 86%, 79%, 73%
SGL31BA	318μm	88%, 82%, 76%
TGP-60-H	192μm	96%, 90%, 82%, 76%

Table 4.1: Measured initial thickness of each sample and compression levels used in permeability experiments

non-woven carbon fibers, and carbon fiber paper. Measurements were taken at multiple levels of compression thought to correspond with typical levels in a fuel cell. The woven carbon fiber sample was Avcarb 1071-HCB (Ballard). The non-woven carbon fiber and paper based samples were SGL31BA (SGL Carbon) and TGP-60-H (Toray). None of the samples contained a microporous layer.

The initial thickness of each type of sample was determined with micrometers. In order to achieve a 'light' pressure on the sample during thickness measurement, load was distributed by a 1" x 1" square of shim stock placed between the micrometer and the sample. Five measurements were taken of each sample type and the average was taken as the initial thickness. The measured initial thickness as well as the compression levels used during permeability experiments is shown in table 4.1.

As described previously, multiple layers of GDL separated by thin spacers were used to increased flowrate and thickness to convenient levels. For all three material types, using four material layers was found to be sufficient. For each four layer sample, pressure-flowrate data was collected. Thickness fractions were incrementally decreased, reusing the sample, until the lowest thickness fraction was reached. Then the samples were replaced and the test was repeated. The test was repeated five times for each material type. Figure 4.4 shows the average permeability for each material type at various levels of compression. The errorbars indicate the 95% confidence interval based on the mean and standard deviation of the five experiments at each level. It was found that the SGL31BA (non-woven) had a very

similar range of permeability as compared to the Avcarb 1071-HCB (woven). This range of permeabilities is surprisingly high considering that Bluemle [4] reports in-plane permeabilities about an order of magnitude lower for 4 different ETEK woven cloth samples. The data indicates that TGP-60-H (paper) has significantly lower permeability than the other materials; its measured range of permeabilities is in good agreement with the range reported by Mathias [14]. Perhaps not surprising is that the woven material shows the most consistency in permeability from sample-to-sample; The non-woven and paper based materials show permeabilities that have a variation in the range of 10-15% of the measured average compared to carbon cloth which shows a range of 5-10%.

One way to model the relationship between porosity and permeability is through the Kozeny-Carman equation [5]

$$k_i = C\frac{\phi^3}{(1-\phi)^2} \tag{4.12}$$

where C is a constant. This equation is ideally suited for low porosity materials where the pores have little interaction with one another. In contrast, 'pores' in the gas diffusion layer are highly connected and have high porosities (typically $> 60\%$). It has been shown that the Kozeny-Carman equation does not always predict the correct behavior of permeability in fibrous media [3]. Therefore, it is interesting to plot the permeability against the porosity (fig. 4.5). The porosity of each experimental data point was estimated from knowledge of the thickness fraction and the porosity at the initial thickness by the equation

$$\phi = 1 - \frac{h_o}{h}(1-\phi_o) \tag{4.13}$$

The value of the initial porosity ϕ_o was obtained from manufacturers specifications. Porosity specifications for Avarb 1071-HCB were not available, so it is omitted for fig. 4.5. Results show that TGP-60-H carbon fiber paper follows the Kozeny-Carman relationship quite closely. However, SGL31BA does not admit a

least-squares fit that falls within the estimated error bounds of the measurement. This is surprising considering that the non-woven material SGL31BA has a similar pore structure to that of the TGP-60-H carbon fiber paper.

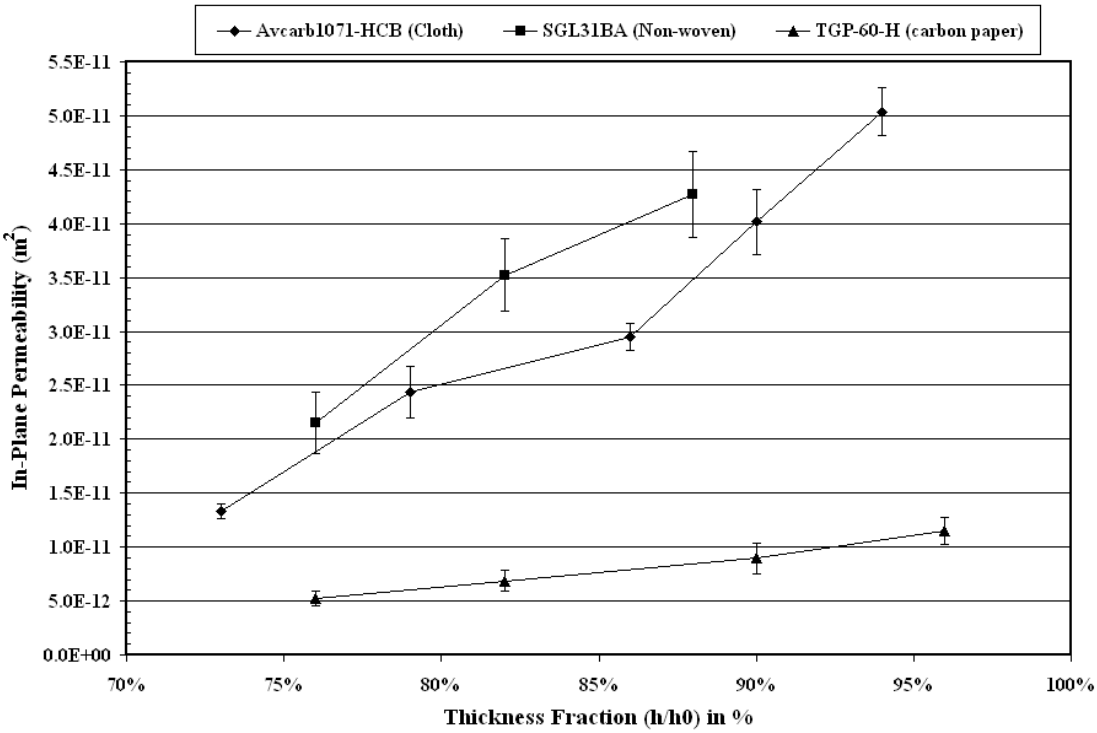

Figure 4.4: In-plane permeability of several GDL

4.5 Conclusions

It has been shown that simple, yet robust radial permeability experiments can be utilized to characterize and differentiate in-plane permeability of gas diffusion layers. These experiments can use either a wetting liquid or a gas of known viscosity as the host fluid and reach identical conclusions. However, flowrates dependence on pressure is different for gases and liquids and must be recognized when large pressure differentials are present. Results on three commonly used gas diffusion

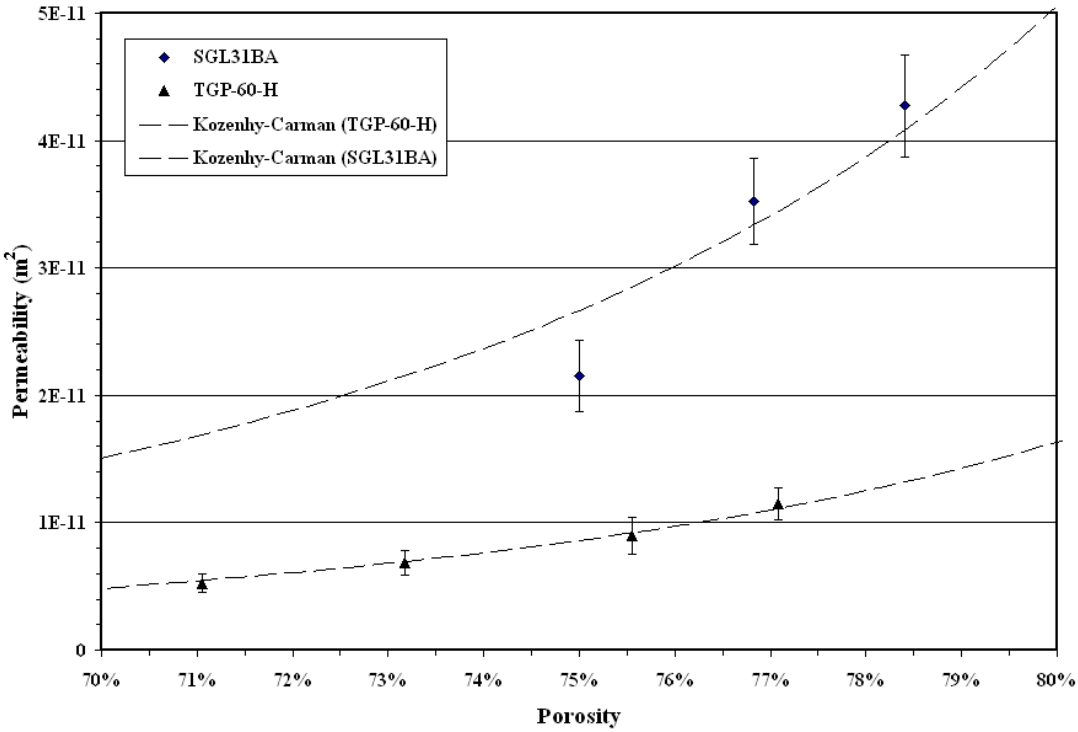

Figure 4.5: Experimentally obtained permeability fitted to the Kozenhy-Carman equation 4.12. The computed constants are $C_{\text{TGP-60-H}} = 1.276 \times 10^{-11}$ m^2 and $C_{\text{SGL31BA}} = 3.952 \times 10^{-11}$ m^2

layer materials show that the non-woven material SGL31BA and the carbon fiber cloth material Avcarb 1071-HCB have in-plane permeabilities substantially higher than those reported for other materials throughout the literature.

Chapter 5

FINAL REMARKS

In chapter 2, we have developed a model which captures the three dimensional physics of channel bypass in serpentine flow fields using a one dimensional formulation which admits a closed form solution. The model was used to show the conditions under which convection can be made the dominant mechanism of mass transport. It was found that the primary parameters which determine this are the in-plane permeability of the GDL and channel length. Thickness of the GDL plays a minimal role in the relative influence of convection.

For reasons stated earlier, the hypothesis has been that increased convection will significantly improve performance. However, a key weakness to the current model is that it cannot easily predict *how much* convection will improve performance. There are two reasons why this is difficult. The first is because the species conservation equation contains the Butler-Volmer equation as either a boundary condition or source term (depending on whether the catalyst layer is modeled as 3D or 2D entity). The Butler-Volmer equation is a non-linear relationship between the current density and surface overpotential and prevents a closed-form solution from being attained with the current model. A second reason is that the velocity streamlines in the GDL never pass through the catalyst layer; instead they are parallel. Thus, diffusion always plays at least a small role in gas transport to the catalyst layer. The utility of the model is that serpentine flow fields can be designed which are known *a priori* to have convective dominance. Then, either experiments

or full computational treatments can be used to determine the effect of convective dominance.

Particle image velocimetry was performed on dynamically similar models of an interdigitated and single-serpentine flow field. Using this technique, velocity fields were obtained at representative cross-sectional locations of the flow channels which shows that the problems associated with observing flows with primary-to-secondary velocity ratios approaching 100-to-1 are surmountable. The velocity fields obtained show channel bypass in both interdigitated (for which its existence is obvious) and serpentine flow fields. A finding of possible significance is that convection into and out of the porous layer does not appear to vary smoothly with location along the channel; this is postulated to be caused by local variations in GDL permeability. Since a similar pore structure was used to that of non-woven and paper based gas diffusion layers, it is thought that this may occur in real fuel cells as well. If this is true, carbon cloth based gas diffusion layers may offer an alternative because they have a pore structure which is more organized. It is not known how or if local variations in velocity into the GDL will affect the performance.

In the serpentine flow field, it was observed that inertial effects can also contribute to convection into the GDL. It may be possible to incorporate such effects into the analytic formulation. For example, Deans vortices which were observed at the turns of the serpentine might be taken into account by the modeling them as a small pressure drops at the turn. Then it will be possible that the velocity through the GDL at the turns is not zero as currently predicted.

While it is tempting to assume that performing PIV on live fuel cell is preferable over dynamically similar models, the latter offers advantages that may justify its continued existence. Even if micro-PIV can be shown to work in live fuel cells, it will not likely be able to observe secondary flows because techniques such as those used in the current study to enable quantification of the cross-sectional view

(thick, high powered light sheets with equally thick depth-of-field) is not possible at very high magnifications; in fact, micro-PIV relies on small depth-of-field to keep out-of-focus particle from disturbing the data. Thus, micro-PIV may give a more realistic flow, but dimensional similarity may be enable more useful phenomenon to be observed.

A measurement technique which improves on the pre-existing methods to measure in-plane permeability was pursues. A model which allows for gas compressibility was developed and validated. Subsequently, the in-plane permeability of gas diffusion layers representing the three major manufacturing techniques were measured. It was found that the cloth and non-woven gas diffusion layer had much higher permeability than the carbon paper. However, since literature suggests that the permeability of cloths can be significantly lower than the that measured in the current study, it is seen that in-plane permeability of clothes is highly dependant on the construction. It is also seen that carbon cloth has the most consistent in-plane permeabilities, although more than five samples would need to be tested to prove this conclusively.

Thus, a cohesive framework for convective flow in fuel cells has been presented. The existence of convection in the form of channel bypass has been predicted and measured. A technique to measure in-plane permeability is presented which should assist with the ability to design fuel cells with increased convective performance.

BIBLIOGRAPHY

[1] P. Argyropoulos, K. Scott, and W.M. Taama. Carbon dioxide evolution patterns in direct methanol fuel cells. *Electrochimica Acta*, 44(20):3575–3584, 1999.

[2] P. Argyropoulos, K. Scott, and W.M. Taama. Gas evolution and power performance in direct methanol fuel cells. *Journal of Applied Electrochemistry*, 29(6):663 – 671, 1999.

[3] B.T. Astrom, R.B. Pipes, and S.G. Advani. On flow through aligned fiber beds and its application to composites processing. *Journal of Composite Materials*, 26(9):1351–1373, 1992.

[4] M. Bluemle, V. Gurau, J. Mann, T. Zawodzinski, E. De Castro, and Y.M. Tsou. Permeability and weetability measurements for gas diffusion layers of PEMFCs. In *Fuel Cell Seminar: Abstracts*, 2004. Poster 53.

[5] P.C. Carman. Fluid flow through a granular bed. *Transactions of the Institution of Chemical Engineers*, 15:150–167, 1937.

[6] W. He, J. Yi, and T.V. Nguyen. Two-phase flow model of the cathode of PEM fuel cells using interdigitated flow fields. *AIChE*, 46(10):2053, 2000.

[7] G. Hu, J. Fan, S. Chen, Y. Liu, and K. Cen. Three-dimensional numerical analysis of proton exchange membrane fuel cells (PEMFCs) with conventional and interdigitated flow fields. *Journal of Power Sources*, 136:1–9, 2004.

[8] A. Jena and K. Gupta. Characterization of porosity of electrodes and seperators in fuel cell industry.

[9] D. Kramer, E. Lehmann, G. Frei, P. Vontobel, A. Wokaun, and G.G. Scherer. An on-line study of fuel cell behavior by thermal neutrons. *Nuclear Instruments and Methods in Physics Research Section A-Accelerators Spectrometers Detectors and Associated Equipment*, 542 (1-3): 52-60(1-3):52–60, 2005.

[10] D. Kramer, J.B. Zhang, R. Shimoi, E. Lehmann, A. Wokaun, K. Shinohara, and G.G. Scherer. In situ diagnostic of two-phase flow phenomena in polymer electrolyte fuel cells by neutron imaging part a. experimental, data treatment, and quantification. *Electrochimica Acta*, 50(13):2603–2614, 2005.

[11] W.K. Lee, C.H. Ho, Zee J.W., and M. Murthy. The effects of compression and gas diffusion layers on the performance of a PEM fuel cell. *Journal of Power Sources*, 84:45–51, 1999.

[12] G.Q. Lu and C.Y. Wang. Electrochemical and flow characterization of a direct methanol fuel cell. *Journal of Power Sources*, 134(1):33–40, 2004.

[13] J. Martin, P. Oshkai, , and N. Djilali. Flow structures in a U-shaped fuel cell flow channel: Quantitative visualization using particle image velocimetry. *Journal of Fuel Cell Science and Technology*, 2(1):70–80, 2005.

[14] M. Mathias, J. Roth, J. Fleming, and W. Lehner. *Handbook of Fuel Cells Fundamentals, Technology and Applications.*

[15] S. McCallum. Fuel for thought: A uvic research team lays the groundwork for a new generation of fuel cells. *Research and Discovery at the University of Victoria*, 5(3), 2005.

[16] M. Mench, C.Y. Wang, and S. Thynell. An introduction to fuel cells and related transport phenomena. *International Journal of Transport Phenomena*, 3:151–176, 2001.

[17] T.V. Nguyen. A gas distributor design for proton-exchange- membrane fuel cells. *Journal of the Electrochemical Society*, 143:105, 1996.

[18] U. Pasaogullari and C.-Y. Wang. Two phas transport and the role of microporous layer in polymer electrolyte fuel cells. *Electrochimica Acta*, 49:4359–4369, 2004.

[19] N. Pekula, K. Heller, P.A. Chuang, A. Turhan, M.M. Mench, J.S. Brenizer, and K. Unlu. Study of water distribution and transport in a polymer electrolyte fuel cell using neutron imaging. *Nuclear Instruments and Methods in Physics Research Section A-Accelerators Spectrometers Detectors and Associated Equipment*, 542(1-3):134–141, 2005.

[20] Pharoah. On the permeability of gas diffusion media used in PEM fuel cells. *Journal of Power Sources*, 144:77–82, 2005.

[21] A.K. Prasad. Particle image velocimetry. *Current Science*, 79(1):101–110, 2000.

[22] A Qi and A. Kaufman. Improvement of water management by a microporous sublayer for PEM fuel cells. *Journal of Power Sources*, 109:38–46, 2002.

[23] Roesgen. Optimal subpixel interpolation in particle image velocimetry. *Experiments in Fluids*, 35(3):252–256, 2003.

[24] S. Shimpalee and S. Dutta. Numerical prediction of temperature distribution in PEM fuel cells. *Numerical Heat Transfer A*, 38:111–128, 2000.

[25] W. Sun, B. Peppley, and K. Karan. Modeling the influence of GDL and flow-field plate parameters on the reaction distribution in the PEMFC cathode catalyst layer. *Journal of Power Sources*, 144:42–53, 2005.

[26] K. Tüber, D. Pócza, and C. Hebling. Visualization of water buildup in the cathode of a transparent PEM fuel cell. *Journal of Power Sources*, 125(2):403–414, 2003.

[27] Um and Wang. Three-dimensional analysis of transport and electrochemical reactions in polymer electrolyte fuel cells. *Journal of Power Sources*, 125:40–51, 2004.

[28] A. Weber and J. Newman. Effects of microporous layers in polymer electrolyte fuel cells. *Journal of the Electrochemical Society*, 152(4):A677–A688, 2005.

[29] P.M. Wilde, M. Mandle, M. Murata, and N. Berg. Structural and physical properties of GDL and GDL/BPP combinations and their influence on pemfc performance. *Fuel Cells*, 3:180–184, 2004.

[30] M. Williams, R. Kuntz, and J. Fenton. Influence of convection through gas-diffusion layers on limiting current in PEMFCs using a serpentine flow field. *Journal of the Electrochemical Society*, 10:1617–1627, 2004.

[31] Yang, Zhang, Lubawy, and Wang. Visualization of liquid water transport in a PEFC. *Electrochemical and Solid-State Letters*, 7(11):A408–A411, 2004.

[32] H. Yang and T.S. Zhao. Effect of anode flow field design on the performance of liquid feed direct methanol fuel cells. *Electrochimica Acta*, 50:3243–3252, 2005.